2017

Finite Element Modeling of the Plantar Fascia: A Viscohyperelastic Approach

Alexander Knapp

Suggested Citation

Knapp, Alexander, "Finite Element Modeling of the Plantar Fascia: A Viscohyperelastic Approach" (2017). *UNF Graduate Theses and Dissertations*. 740.
https://digitalcommons.unf.edu/etd/740

Finite Element Modeling of the Plantar Fascia: A Viscohyperelastic Approach

By

Alexander Matthew Knapp

A Thesis submitted to the Department of Mechanical Engineering

in partial fulfillment of the requirements for the degree of

Master's of Science in Mechanical Engineering

UNIVERSITY OF NORTH FLORIDA

COLLEGE OF COMPUTING, ENGINEERING, AND CONSTURCTION

April 2017

This Thesis titled Finite Element Modeling of the Plantar Fascia: A Viscohyperelastic Approach is approved:

Alexandra Schönning, PhD
Thesis Advisor and Committee Chairperson

Stephen Stagon, PhD
Committee Member

Beven Livingston , PhD
Committee Member

Accepted for the School of Engineering:

Murat Tiryakioglu, PhD, CQE
Director of the School of Engineering

Accepted for the College of Computing, Engineering, and Construction:

Mark Tumeo, PhD, JD, PE
Dean of the College of Computing, Engineering and Construction

Accepted for the University:

John Kantner, PhD
Dean of the Graduate School

Acknowledgements

I would like to begin by first and foremost thanking Dr. Alexandra Schönning for her guidance and support during the creation of this thesis as my primary thesis advisor. I am deeply indebted to her for her patience and dedication to my education, ensuring that I learn the proper tools and techniques to flourish in the academic world. Without her assistance, I am certain that this project would not have been completed as quickly or successfully as it was. I am grateful to have had such a mentor through this process, and I hope to be able to continue to grow with her guidance as I go forward in my academic career.

I would also like to thank Dr. Stephen Stagon for being one of the first to notice any talent I may have and for giving me my first research opportunities, as well as giving me invaluable feedback with this project. I would not be on this path without the guidance he gave me early on.

I am also thankful for the guidance of Dr. Beven Livingston during this project, especially in the early parts of the project when I was a novice in the anatomy of the human foot and all its many intricacies. Her knowledge helped me to develop accurate geometries that have led to a successful project, and hopefully many more works in the future.

While not a member of my thesis committee, I am also grateful for the input that Dr. Grant Bevill has given me throughout my final semester pertaining to my thesis and my career as a whole. I sincerely hope to collaborate with him going forward into my academic career.

I also cannot begin to express my gratitude to Dr. Murat Tiryakioglu and Dr. Mark Tumeo (and the College of Computing, Engineering, and Construction as a whole) for funding my tuition as well as for all of the many opportunities they have given me during my time as a Master's student at UNF. Getting the chance to teach courses and be a teaching assistant for many others have allowed me to figure out first hand that a career in academia as a professor is what I wish to pursue. The School of Engineering has given me so much, and I will never be able to repay it.

I would also like to extend a most sincere thank you to Dr. Cara Tasher, Professor Tommy Shapard, and the UNF Choral department for providing me with an outlet to keep my stress levels relatively low during the last two years. They have shown me that I can, in fact, be both a successful engineer and musician, and I am thankful to have had the chance to discover this. This project would have been much harder without the break that singing has given me, and so I extend my deepest thanks to them.

Lastly, I must thank my closest friends and family for their support during this project. Scott, Chelsea, and Joey, the three of you helped me out in my darkest times and I would not have made it through these years as the confident and enthusiastic person I came in as without you. To my brother Andrew and my future sister-in-law Sammi, I thank you for being two of my closest confidants and friends in these last two years. Lastly, I would absolutely never have gotten this far without the love and support of my mom and dad, Judi and Clay Knapp. You both inspire me to be the greatest version of me I can be. I love you all more than you can fathom.

Table of Contents

List of Figures

List of Tables

Abstract

The present work details the creation and analysis of a finite element model of the foot, wherein the plantar fascia was modeled as a viscohyperelastic solid. The objective of this work was to develop a fully functional CAD and Finite Element Model of the foot and plantar fascia for analysis by examining the transient stresses on the plantar fascia through the use of a viscohyperelastic material model. The model's geometry was developed through the use of image processing techniques with anatomical images provided by the National Institutes of Health. The finite element method was used to analyze the transient response of the plantar fascia during loading. As a first step towards modeling the transient response of the mechanical behavior of the plantar fascia under dynamic loadings, standing conditions were used to analyze the relaxation of the plantar fascia over a time period of 120 seconds (which is the steady-state relaxation time of the plantar fascia). This study resulted in a fully functional model with transient stress data on the behavior of the plantar fascia during loading, along with stress and deformation data for the bones and soft tissue of the foot. The results obtained were similar to that recorded in literature. This model is the first step towards fully characterizing the mechanics of the plantar fascia so as to develop novel treatment methods for plantar fasciitis, and can be applied to future studies to develop novel orthotic devices and surgical techniques for the treatment of and prevention of plantar fasciitis.

Chapter 1. Background Information

1.1. Introduction

Biomechanics is a relatively new branch of mechanics that seeks to characterize the mechanical behavior of biological systems. In recent years, finite element modeling has become a preferred tool for the mechanical analysis of biological systems due to the complex material models that often occur in such systems. The human foot has become a major topic of interest for researchers due to the complex geometry and loadings it can experience in day-to-day activities. The objective of the present work is to develop a functional finite element model of the foot, with a special focus on modeling the plantar fascia as a viscohyperelastic solid, and present the results of the finite element model under static loading conditions.

The plantar fascia is a major structural component of the foot. It is a highly fibrous structure that originates from the tuberosity of the calcaneus and extends outward in a fan-like structure to the distal ends of the metatarsals, supporting the arch of the foot formed by the calcaneus and metatarsal bone as shown in Figures 1 and 2.

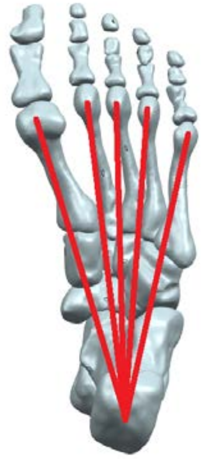

Figure 1: Fan-Like Structure of the Plantar Fascia

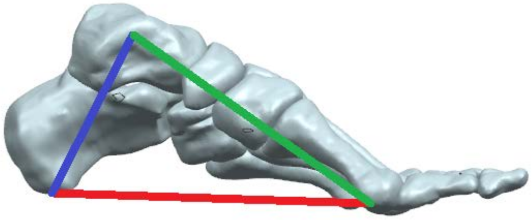

Figure 2: The Human Foot as a Truss

According to Kim and Voloshin, the plantar fascia has been observed to carry approximately 14% of the weight applied to the foot (or 14% of half the weight of the body) while standing [1].

Plantar fasciitis is an inflammatory condition of the plantar fascia that is characterized by intense pain, typically at the heel, when weight is applied to the foot; in particular, this pain is often at its peak after prolonged periods of rest [2]. This condition affects approximately two million Americans annually, accounts for around 15% of all foot related medical complaints, and is the cause of discomfort for roughly 8-19% of the medical complaints of pain in the foot by athletes [3, 4, 5]. This condition is often treated with physical therapy; however, for the most extreme cases, surgical release of the plantar fascia is performed [6]. However, according to Gefen this tends to increase the stresses throughout the rest of the foot by upwards of 200%, and is not an ideal solution [6].

Because of the number of people plantar fasciitis affects, computational analysis of the plantar fascia using the finite element method has become of interest to researchers so that advancements can be made in the field of diagnosis and treatment of plantar fasciitis. Due to the fibrous nature of the plantar fascia as a biological tissue, the plantar fascia has been shown in literature to exhibit nonlinear elasticity and viscous behavior, thereby requiring complicated material models to accurately describe the mechanics of the plantar fascia [7, 8]. While several finite element models of the foot have been made under various material property assumptions and loading conditions, a finite element model that examines the viscous behavior of the plantar fascia has yet to be created. The present work details the creation of a finite element model of the foot with the plantar fascia as a viscohyperelastic solid.

1.1. Literature Review

1.1.1. Summary of Previous Works on the Mechanical Behavior of the Plantar Fascia

Early theoretical and finite element models of the human foot, such as that of Kim and Voloshin, Jacob et al. and Chu et al., relied on simplified geometry and material assumptions (such as linear elasticity) due to computational barriers that limited the accuracy the models could produce [1, 9, 10]. The work of Kim and Voloshin is exceptionally important, as, despite the simplifications of the model, a clear link between the stresses on the bones of the foot and the plantar fascia was established by analyzing the arch of the foot both with and without the plantar fascia in the model [1]. Models such as these built a foundation for future models to come, but are largely antiquated in comparison to modern works, which now often use complex geometry and advanced material models such as the hyperelastic Mooney-Rivlin model. One of the first notable experimental studies was that presented by Carlson et al., which investigated the complex relationship of the dorsiflexion angle (angle at which the phalanges of the foot are rotated), loading of the Achilles' tendon, and stretch of the plantar fascia in an in-vitro setting with cadaver specimens [7]. This is one of the first studies that also shows a non-linear elastic behavior in the plantar fascia, thereby establishing that a non-linear elastic material model will be needed to get the most accurate results possible when analyzing the plantar fascia. Another experimental study by Huerta et al. further illustrated a relationship between BMI (body mass index) and the thickness of the plantar fascia to the strain under loading [11]. Similarly, the works of Yu et al. and Spears et al. investigated the effect of heel elevation and loading mechanism on the stresses of the foot respectively, again showing a correlation between the structure of the foot and the stresses felt throughout [12, 13]. This also implies that the results obtained in a finite element simulation will be highly dependent on the orientation of the foot and how much weight is applied to the foot, which is something to be conscious of going forward.

As technology has advanced, the ability to create highly detailed geometrical models for computational analysis has become apparent. Most commonly, medical images, such as those of Computed Tomography (CT) scans, are used to generate models by stacking images on top of each other to create CAD models that can be used for analysis, such as the models presented by Camacho et al., Knapp et al., and Jackson [14, 15, 16]. The methodologies used in these publications to create 3-D geometries from 2-D images will form the basis for the creation of the geometrical model used in this work.

With sufficient computational power available, the finite element method has become an increasingly popular choice for studies on the mechanical behavior of the foot and plantar fascia. For instance, Cheung et al. investigated the effects of stiffening the soft tissue on the overall stresses throughout the foot using the finite element method [17]. Interestingly, stiffening the soft tissue led to an increase in the stresses throughout the foot, again indicating that the stresses on the foot will vary from person to person, as no single person’s biological makeup is the same as another’s. This particular experiment modeled the soft tissue as hyperelastic, but used a linearly elastic material to model the plantar fascia, making the results for the stretch of the plantar fascia less accurate. A similar study by the same author investigated the effects of stiffening the plantar fascia (albeit as a linearly elastic material) using the finite element method [18]. Unlike with the soft tissue, increasing the stiffness of the plantar fascia led to a reduction of stress throughout the foot, which falls in line with the notion that surgical removal of the plantar fascia increases stresses throughout the foot as found in literature [6]. Carlson et al.’s experimental work was followed by Cheung et al. and Cheng et al. with finite element models of the mechanical response of the plantar fascia during both Achilles' tendon loading and dorsiflexion [19, 20]. The strengths of these models were that they modeled the encapsulating soft tissue as hyperelastic; however, other support structures (including the plantar fascia) were modeled as simple tension-only elements that were only linearly elastic. Building on those models, Cheng et al. and Antunes et al. analyzed the plantar fascia as a non-linear solid; as such, these publications contain the most complete models for analyzing the mechanical behavior of the plantar fascia as an elastic material with no viscous properties [2,21]. Each of these models presents something unique, and all give valuable insight into what is required to create an accurate model of the foot. For instance, the use of tension only 1-D elements is common throughout all the finite element models for tendons, which will similarly be used in the present work. The most accurate models used a Mooney-Rivlin solid to describe the non-linear behavior of the plantar fascia, while Natali et al. proposed a new constitutive model of the plantar fascia that split the behavior of the collagen fibers in the plantar fascia and the surrounding protein matrices into separate components [22]. While the present work will use the Mooney-Rivlin model so as to remain consistent with previous works, future investigations should perhaps consider models such as the one presented by Natali et al. In addition, other works, such as those by Sconfienza et al., Wu et al., and Jiang et al., seek to further quantify the in-vivo response of the plantar fascia using sonoelastography, which is still largely in its infancy for developing practical models for finite element modeling, but could be considered for future models [23, 24, 25].

While the modeling of the plantar fascia as an elastic solid has been well investigated, the plantar fascia is also known to exhibit viscoelastic properties as observed by Chaudhry et al. and Pavan et al. [26, 27, 28]. The work of Chaudhry focused on predicting the stresses of various fascia of the body using relaxation spectra techniques developed by Y.C. Fung [29]. Conversely, the work of Pavan et al. focused on the relaxation of the plantar fascia under constant strain, and developed a constitutive model of the viscohyperelastic behavior of the plantar fascia based on the model developed by Holzapfel [30] for rubber materials. The models investigated by Pavan and Holapfel are of particular note, as a similar constitutive model will be used due to the built in features of the chosen analysis software, NX, developed by Siemens [31].

It is clear from this review that much of the work required to get a truly accurate model of the human foot and plantar fascia has been performed. However, no model has analyzed the transient behavior of the plantar fascia in a practical loading situation. With the transient behavior of the plantar fascia quantified through more accurate finite element modeling techniques, new insights into the treatment and prediction of plantar fasciitis can be discovered.

1.2.2. Theory

1.2.2.1. Anatomy of The Foot

The human foot is made up of twenty-six bones, the plantar fascia, the Achilles' tendon, ligaments, articular cartilage, and several layers of soft tissue, as any anatomy reference, such as that written by Henry Gray, will indicate [32]. Figure 3 illustrates and labels the bones of the foot, including the distal segments of the tibia and fibula (bones of the lower leg).

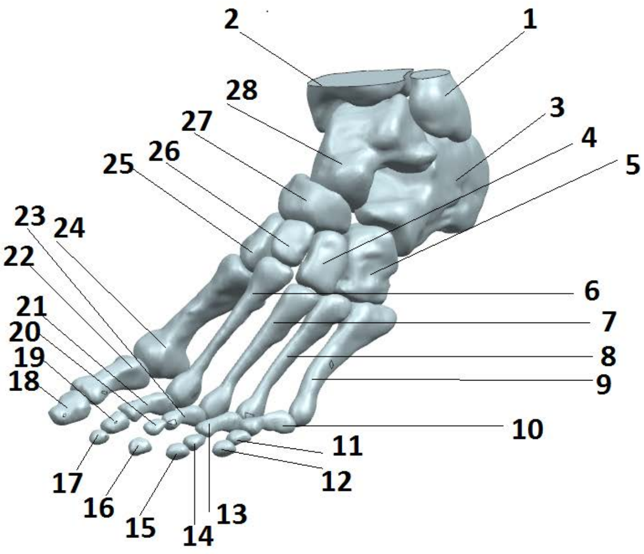

Bone	Number(s)
Fibula	1
Tibia	2
Calcaneous	3
Lateral Cuniform	4
Cuboid	5
Second Metatarsal	6
Third Metatarsal	7
Fourth Metatarsal	8
Fifth Metatarsal	9
Phillanges	10-23
First Metatarsal	24
Medial Cuniform	25
Middle Cuniform	26
Navicular	27
Talus	28

Figure 3: Anatomy of the Human Foot

As previously described, the plantar fascia is a fibrous structure that connects the calcaneus to the metatarsals as the third member of a truss. Like many soft tissues of the human body, the plantar fascia exhibits non-linear elastic properties largely due to the unfolding of collagen fibers under loading as described by Pruitt et al. [33]. This makes even a simple analysis of the plantar fascia under loading more complicated than a typical engineering problem.

The bones of the foot are comparatively rigid-like structures that support the body in its day-to-day activities. Created out of layers of hydroxyapatite stacked on collagen fibers, bones of the human body are generally linearly elastic structures for small strains, with slight variations in the stiffness between tension and compression [33]. It should be noted that bones are made out of two structures, trabecular and cortical bone. These structures have different mechanical properties; however, it is quite common in literature to model the bones as one structure with a Young’s modulus that averages the Young’s modulus of the two bone structures together [17]. For ease of modeling as well as being consistent with literature, a similar approach was taken in the present work.

The loading of the body carried through the tibia and fibula is transferred between bones via cartilage and ligaments. Cartilage acts as a form of barrier between bone structures, absorbing compressive loadings and lubricating bones so that they can glide over each other with minimal friction [33]. Ligaments carry tensile loading between bones, playing a critical role in ensuring that the foot keeps the proper structure [33]. Of special note is the Achilles' tendon, which carries approximately 50-75% of the weight of the foot upwards from the calcaneus to the calf muscles of the leg as reported in literature [18, 19, 32]. Finally, the structures of the foot are surrounded by soft tissue. Traditionally, the soft tissue elements (skin, fat pad, and deep muscle tissues) are lumped together as one hyperelastic structure [20].

1.2.2.2. Hyperelasticity

For all mechanical models, it is important to take the constitutive model used into consideration, as indicated by Martins et al.'s work which illustrates that the type of model used can lead to very different results in the long run when it comes to hyperelastic materials [34]. Many biological materials, such as soft tissue and the plantar fascia, exhibit non-linear behavior within their elastic regions due to the unfolding of collagen fibers when loading is applied [33]. Figure 4 illustrates what non-linear Stress versus Strain curve for uniaxial tension might look like.

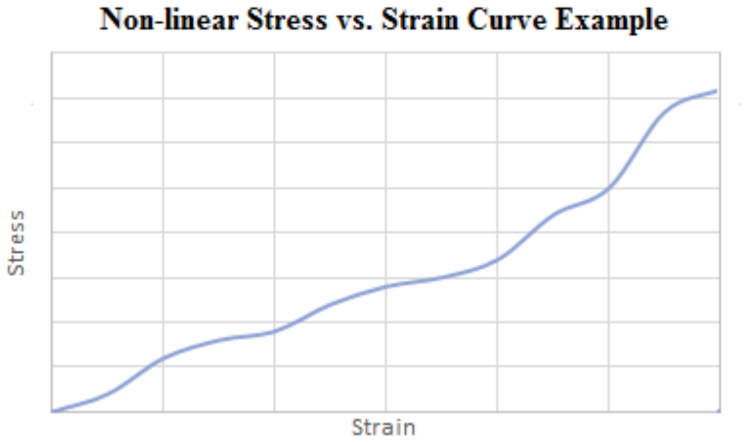

Figure 4: Non-Linear Elasticity Example Plot

This causes common engineering assumptions of linear elasticity to be highly inappropriate for the analysis of such materials. Consequentially, standard engineering equations such as Hooke’s Law are unsuitable to use. However, a relationship between the stress and strain can still be found. This is typically done through the use of strain energy density methods. In principle, the strain energy density (W) is defined as the internal energy put into the system under loading, and represented by equation (1) in its simplest form for axial loading:

$$W(\epsilon) = \int \sigma d\epsilon \tag{1}$$

Where ϵ is the strain in the axial direction for this example. Consequentially, this definition means that the stress can be found by taking the derivative of the strain energy density with respect to strain. In many cases for non-linear materials, the strain energy density is not known, and so it has to be assumed. To account for the non-linear behavior in materials such as rubber and soft tissues, hyperelastic material models are commonly used. Malvern defines a hyperelastic material as such if “There exists an elastic potential function W (or strain-energy function), a scalar function of one of the strain or deformation tensors, whose derivative with respect to a strain component determines the corresponding stress component [35].” In other words, for a defined strain energy density W, the stress can be found by taking the derivative of the strain energy with respect to a deformation measurement, such as strain, such that:

$$\sigma = \frac{dW(\epsilon)}{d\epsilon} \tag{2}$$

This definition allows for the analyst to define the strain energy function as required to match that of the material’s behavior. For the plantar fascia and the encompassing soft tissue of the foot, the Mooney-Rivlin hyperelastic model is commonly used throughout literature. The Mooney-Rivlin model, proposed by Melvin Mooney [36] and Ronald Rivlin [37], uses a strain energy density that defines the internal energy under loading to be a function of the first and second strain (ϵ_{ij}) invariants (I_1 and I_2) and volumetric strain ratio (J), such that:

$$W(I_1, I_2, J) = \sum_{i,j=0}^{n} C_{ij}(I_1 - 3)^i (I_2 - 3)^j + \sum_{k=1}^{m} D(J-1)^{2k} \tag{3}$$

Where,

$$\epsilon_{ij} = \begin{bmatrix} \epsilon_{11} & \epsilon_{12} & \epsilon_{13} \\ \epsilon_{21} & \epsilon_{22} & \epsilon_{23} \\ \epsilon_{31} & \epsilon_{32} & \epsilon_{33} \end{bmatrix} \tag{4}$$

$$I_1 = tr\left(\epsilon_{ij}\right) \tag{5}$$

$$I_2 = (tr\left(\epsilon_{ij}\right)^2 - tr(\epsilon^2) \tag{6}$$

$$J = \det(F) \tag{7}$$

$$F = \frac{dx_i}{dX_j} \tag{8}$$

Where F is the deformation gradient, x_i is a spatial coordinate point after deformation, X_j is a material or reference coordinate point in the reference configuration, and C_{ij} and D are experimentally found material constants that relate to the deviatoric (shape deforming) and dilatational (volume deforming) portions of the strain energy, respectively that are analogous in function to the function of Young's modulus in Hooke's Law. The summing values of n and m are left up to the user; with more terms, the energy function will be more accurate, but more computationally intensive.

This strain invariant definition is convenient to use in the Mooney-Rivlin model as invariants are reference frame indifferent, producing the same result regardless of the reference frame used. In addition, this model, this material model can be used under both finite and infinitesimal strain formulations. By default, the chosen analysis software, NX 10.0, uses finite (large) strain formulations for its hyperelastic materials, such that the strain is defined as below (in spatial coordinates) [31]:

$$\epsilon_{ij} = \frac{1}{2}\left(\frac{du_i}{dx_j} + \frac{du_j}{dx_i} - \frac{du_k}{dx_i}\frac{du_k}{dx_j}\right) \tag{9}$$

Where u_i is the displacement vector between the reference coordinate vector X_i and the deformed position coordinate x_i. This will lead to more accurate results (albeit more computationally intensive ones) than small strain formulations would. One noteworthy final observation is that for an incompressible material, $J = 1$, causing the rightmost term to go to zero, greatly simplifying the model. This assumption will be used for modeling the plantar fascia, as is common throughout literature, such as in [20]. The Mooney-

Rivlin model can also be reformulated such that the invariants are in terms of the principle stretch values as shown below.

$$W(\lambda_1, \lambda_2, \lambda_3) = \sum_{i,j=0}^{n} C_{ij}[(tr(\boldsymbol{\lambda_k}))(\tfrac{1}{2}\Big(\big(tr(\boldsymbol{\lambda_k} - 1)\big)^2 - \big(tr(\boldsymbol{\lambda_k} - 1)^2\big)\Big) - 3\Big))] \quad (10)$$

$$\lambda_k = \epsilon_k + 1 \quad (11)$$

By the definition set by Malvern, the strain energy function can be used to derive the stress tensor in terms of the principle stretches as follows:

$$\sigma_p = \lambda_p \frac{dW}{d\lambda_p} \ (no\ summation) \quad (12)$$

For the case of incompressible uniaxial tension, $\lambda_2 = \lambda_3 = \frac{1}{\sqrt{\lambda_1}}$ in order to meet the incompressibility requirement of J=1, allowing for the values of C_{ij} to be found using experimental tensile data of the stretch of the material.

1.2.2.3. Viscoelasticity

Hyperelastic material models are useful tools for materials in which the mechanical behavior does not vary significantly with time. However, some materials, such as the plantar fascia, are known to exhibit significant time dependent behavior, requiring additional formulation in order to fully quantify the behavior of the material under loading. Viscoelastic materials are defined by the ability for the structural properties to change with respect to time (in the case of biological materials due to the changing structure of fibers and proteins under loading), either by hysteresis, creep, relaxation, or any combination of those phenomena in a manner that shares characteristics of solids and fluids [29, 33]. To illustrate how a material's behavior can change with respect to time more definitively, consider Figure 5 that illustrates one way in which a material's stiffness can change over time under loading.

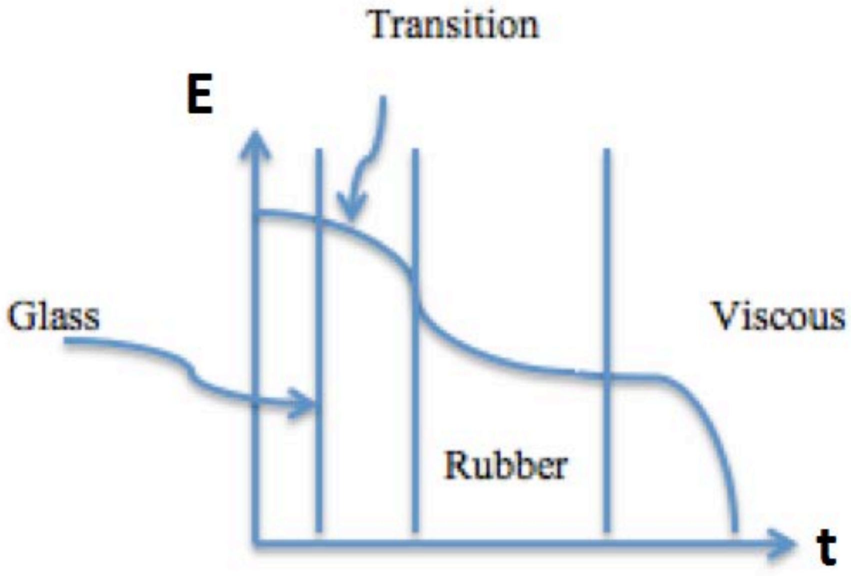

Figure 5: Illustration of an Elastic Response Changing Over Time [33]

Note how under quick loading times the material behaves in a glass-like manner, and softens and eventually acts in a viscous, fluid-like manner as time progresses. In order to quantify the viscoelastic behavior of a body such as the plantar fascia, first consider a body that can be described with the 1-D rheological model presented in Figure 6 [31]:

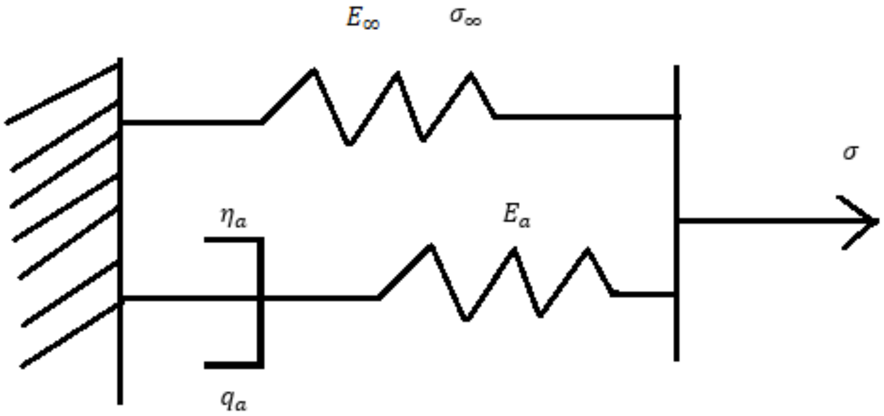

Figure 6: Standard Linear Solid Model [31]

where the top branch represents the steady-state behavior of the model with elastic modulus E_∞ and steady state stress σ_∞, and the lower chain represents the transient behavior of the model with dashpot nomination η_a and transient stress q_a, where the subscript a represents an a^{th} dashpot chain. This model, commonly referred to as a standard linear solid (SLS), forms the basis for the theory of viscoelasticity used in the present work. An SLS is ideal for modeling viscoelastic materials because it is able to model the effects of creep (increasing strain on a body under constant stress loading) and relaxation (decreasing stress when a body is subjected to a constant strain), which are both often present in viscoelastic materials.

Under quasi-static loading conditions, an expression for the total stress throughout the element can be formulated for any N amount of dashpot chains as follows:

$$\sigma_{total} = \sigma_\infty + \sum_{a=1}^{N} q_a \tag{13}$$

This formulation indicates that the total stress throughout the model is made up of both a transient and steady-state component, which are independent from each other. Defining a time constant, τ, as in Equation 14,

$$\tau = \frac{\eta}{E_a} \tag{14}$$

And assuming the strain energy density function of the transient response of the dashpot chains (W_a) can be characterized such that

$$W_a(t) = \beta_a W_\infty \tag{15}$$

Where β is proportionality constant between the transient strain energy density and the steady-state strain energy density, the stress through the SLS can be formulated as below by substituting equations 14 and 15 into equation 13, both in differential equation and convolution forms [30, 31]:

$$\dot{q_a} + \frac{q_a}{\tau_a} = \beta_a \dot{\sigma_\infty} \tag{16}$$

Here τ represents a time constant that relates to the amount of time needed to reach steady state (wherein the dashpot element drops out and only the elastic spring component remains) and β is a unit-less proportional constant that dictates the difference between the initial and steady state stress and strain values throughout the body under loading, and t' is the subsequent time value past the time, t. If relaxation data such as that of Figure 7 for a body under constant strain is obtained such that the elastic (steady-state) stress value is constant and known, experimental values of β and τ can be found using the numerical approximation of Equation 16 by curve fitting the equation to the relaxation data plot [31].

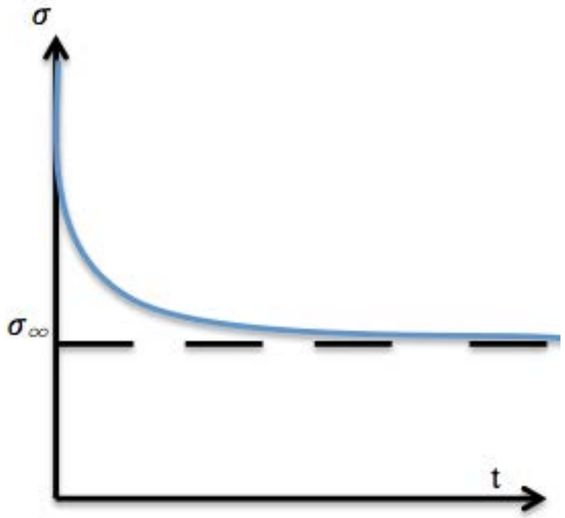

Figure 7: Relaxation Plot Example

$$q_a^{t+\Delta t} = e^{-\frac{\Delta t}{\tau_a}} q_a^t + \beta_a \left(\frac{1-e^{-\frac{\Delta t}{\tau_a}}}{\frac{\Delta t}{\tau_a}}\right)(\sigma_\infty^{t+\Delta t} - \sigma_\infty^t) \qquad (16)$$

This equation relates the transient stress at a time $t + \Delta t$ to a previous stress value at time t. With known values of β and τ, the transient portion of the viscoelastic response is known.

1.2.2.4. Viscohyperelasticity

The section on viscoelasticity made no statement as to the behavior of the steady-state chain of the SLS (recalling that the steady-state portion is represented by the top chain of the SLS in Figure 5). For the case of the plantar fascia, the elastic portion of the SLS must be considered to be non-linear, requiring the use of hyperelastic strain energy functions to be used as opposed to a linear Young's modulus of E_∞. Considering again the idea of the SLS of Figure 5, the viscohyperelastic material model proposed by

Holzapfel, which will be used for the plantar fascia, has a strain energy function of the following form:

$$W(\lambda, t) = W(\lambda)_{elast} + W(t)_{transient} \tag{18}$$

This formulation is such that the elastic and viscous components are independent of each other, where the elastic (steady-state) portion is only a function of strain and the transient strain energy density is a function of time [30]. While the previously discussed rheological model is 1-D, it can still be used such that the stresses are 3-D as in Equation 19.

$$\sigma_{ij} = \sigma_{\infty} + Q_{ij} \tag{19}$$

Defining the 3-D transient stress tensor as Q_{ij} and using the definition set by Malvern with a Mooney-Rivlin model as described in the hyperelasticity theory section to substitute for the value of σ_{∞}, the stress on a point of a viscohyperelastic solid is approximated by the below equation:

$$\sigma_{ij}\left(\lambda_{ij}, t\right) = \lambda_{ij}\,\frac{dW_{elast}(\lambda_{ij})}{d\lambda_{ij}} + Q_{ij}(t) \tag{20}$$

Where:

$$W_{elast}(\lambda_1, \lambda_2, \lambda_3) = \sum_{i,j=0}^{n} C_{ij}[(tr(\boldsymbol{\lambda_k}))(\frac{1}{2}\Big((tr(\boldsymbol{\lambda_k} - 1))^2 - (tr(\boldsymbol{\lambda_k} - 1)^2)\Big) - 3\Big))] \tag{21}$$

As in the original Mooney-Rivlin equation shown in (3), i and j can be summed to an amount of n terms, depending on the accuracy desired by the user. The left term on the right hand side of equation (20) represents the steady-state stress for a given stretch value, and the rightmost term represents the transient stress at a time t. Q_{ij} can be numerically approximated in a manner similar to that of the 1-D model such that [31]:

$$Q_{ij_a}^{t+\Delta t} = e^{-\frac{\Delta t}{\tau_a}} Q_{ij_a}^{t} + \beta_a \left(\frac{1-e^{-\frac{\Delta t}{\tau_a}}}{\frac{\Delta t}{\tau_a}}\right)\left(S_\infty^{t+\Delta t} - S_\infty^{t}\right) \tag{22}$$

Where i and j represent the indices of a transient stress tensor Q_a on an a^{th} chain of the SLS. As with the 1-D approximation, this equation allows for the approximation of a transient tress at time $t + \Delta t$, where S_∞ is the steady-state second Piola-Kirchoff stress, and β and τ are the viscous parameters defined in the 1-D example. With the values of $C_{ij}, \beta,$ and τ known, the complete viscohyperelastic behavior of the plantar fascia can be quantified using the above formulations.

Chapter 2. Research Methodology

2.1. Overview

The creation of a workable finite element model required several sequential steps to be taken. First, anatomical image data was acquired and processed using image thresholding techniques. The resulting images were used to create rough 3-D models that required additional refinement to be used. After refinement, a final assembly that was ready for finite element modeling was created. With the model assembled, appropriate loading and boundary conditions were applied, and the model was solved and analyzed. Figure 8 visually summarizes the process taken to obtain the stress and deformation results of the present work. The overall geometry creation and refinement process is based on that of Schönning et al. [38].

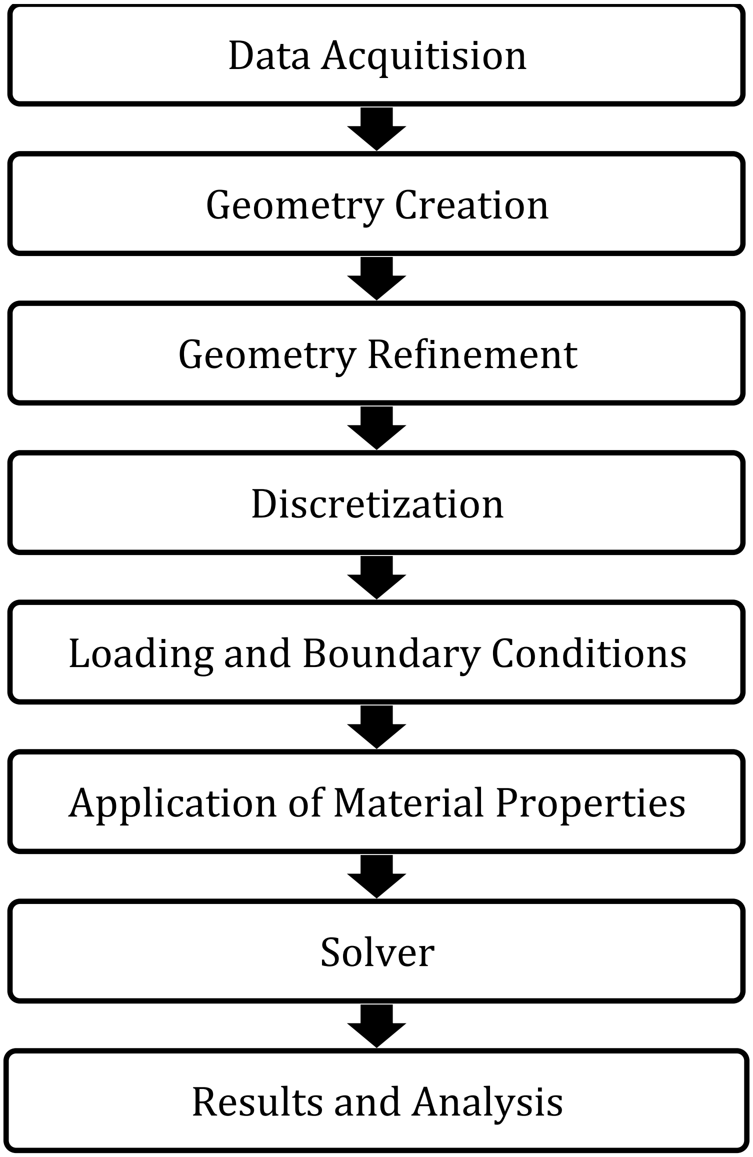

Figure 8: Research Methodology Flowchart

2.2. Geometry Creation

2.2.1. Data Acquisition

To create the complex geometry required for the present study, anatomical images were used to create 3-D models by stacking them on top of each. Images were first obtained from the National Institutes of Health via the Visible Human Project, an initiative created so that anatomical images were available for researchers free of charge [39]. The transverse-axial images used have a resolution of 2048x1216 pixels taken at 1 mm intervals between image slices. For the current study, the lower 279 images of the full body set were used, so as to be able to obtain the anatomy of the foot, including a total of 28 bones, the plantar fascia, and the encompassing soft issue. These image slices were further edited to include only the left foot.

2.2.2. Image Processing and Geometry Generation

For each bone, as well as the soft tissue and plantar fascia, the images were edited using the image processing software FIJI [40]. Each bone was manually edited to be the only bone present on the image set. Figure 9 demonstrates this process for the first metatarsal on one slice.

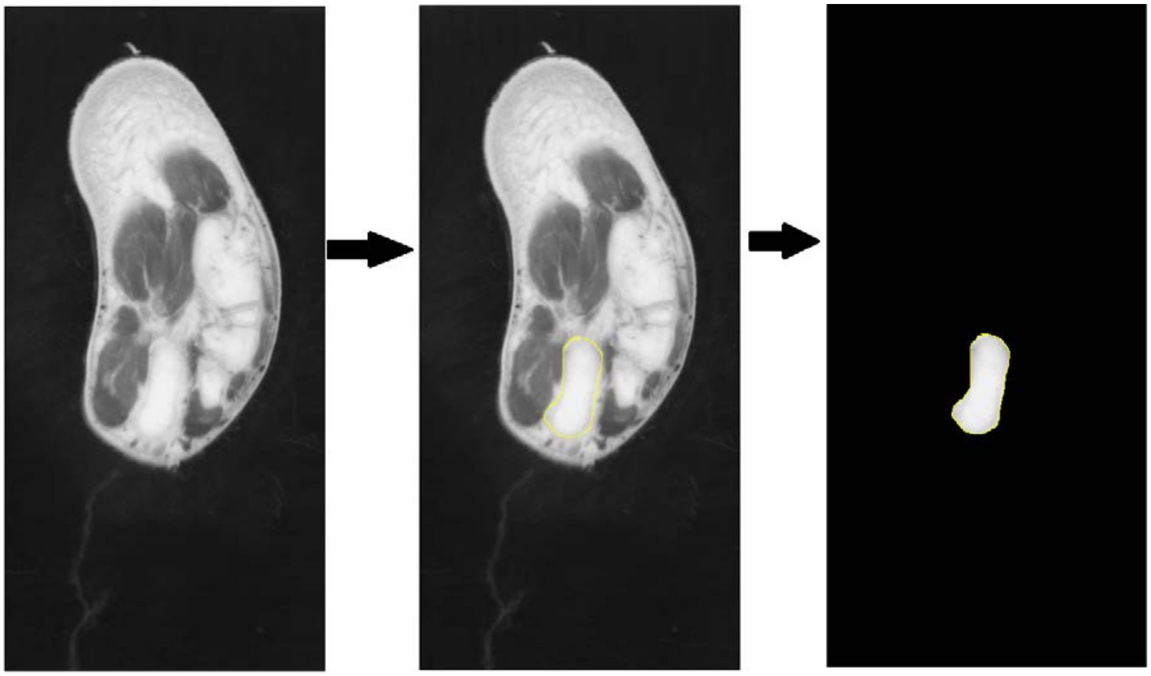

Figure 9: Image Editing Process

After editing each slice, color threshholding was applied to each slice as shown below. This process was done through a mostly visual means, adjusting the threshold as necessary to remove surrounding cartilage and fill holes in the image as represented by Figure 10.

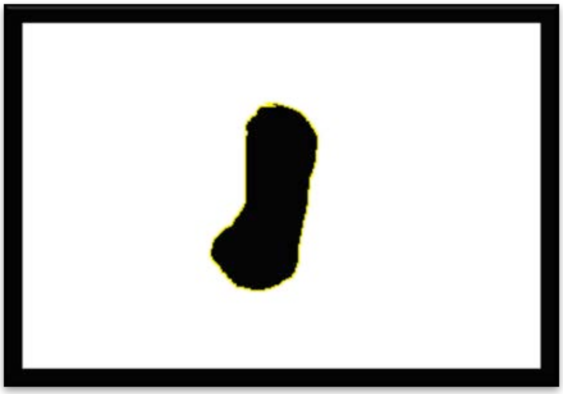

Figure 10: Threshholded Slice

Next, an appropriate scale had to be set so that the models were the proper size. Based on the average foot length of 24.2 cm recorded by Cheng et al. [20], a scale of 29.7521 pixels per centimeter was used, with a voxel depth of 1 mm to match that of the slice intervals. Applying these scales and stacking the slices for each bone resulted in rough models such as that depicted below in Figure 11.

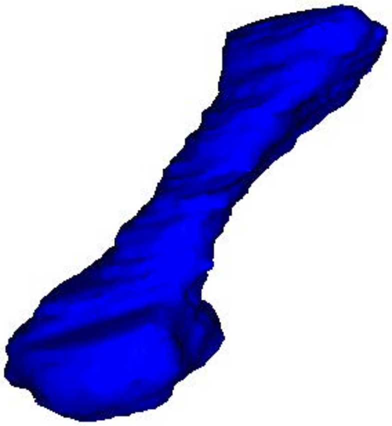

Figure 11: Rough Model Illustration

In this form, the models were unacceptable for analysis due to the rough surface textures and sharp edges present, and so further refinement was performed.

2.2.3. Geometry Refinement

In order to clean the models created by FIJI, the reverse-engineering software Geomagic was used [41]. To begin the refinement process, the software's auto-cleaning process was first used, followed by further cleaning operations to patch holes and smooth the surfaces. This led to much more refined models such as that shown in the Figure 12.

Figure 12: Refined Model Example

Following the initial clean-up procedure, additional detail was focused on refining the surfaces of the models to be smoother so that they were more suitable for finite element meshes, as well as filling any holes that were created in the initial model generation process. Following the refinement process, each model was processed as a Non-Uniform-Rational-B-Spline (NURBS). A NURBS surface can be thought of as a curve that approximates geometry through segmented curves that connect together to form a complete surface as described in literature by Hollister [42]. The resulting NURBS surface CAD model for the first metatarsal is depicted in Figure 13.

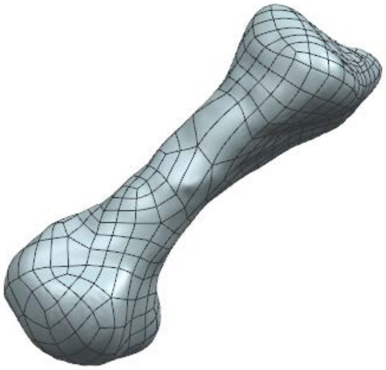

Figure 13: NURBS Surface

Each model was then exported as a .stp file to the analysis software of choice, NX.

This process was similarly carried out for the plantar fascia and soft tissue. The plantar fascia required significant editing to be in a usable form. Due to the orientation of the anatomical images causing the plantar fascia to appear in hard to follow ways, exporting from FIJI led to the broken model shown in Figure 14.

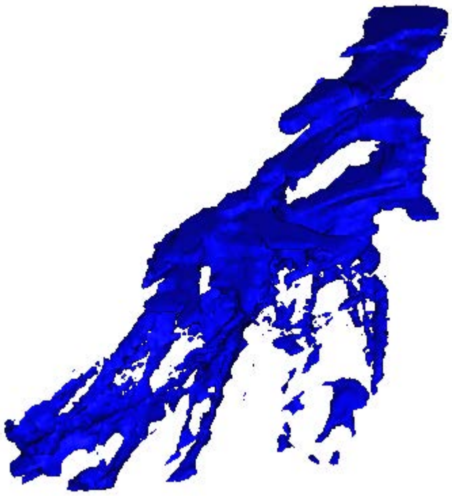

Figure 14: Broken Plantar Fascia Model

This model was manually edited using Geomagic, first by removing the broken sections from the mid-foot extending to the metatarsals, and then manually extruding the remaining geometry outwards to the metatarsals, and then thickened in the narrower regions to create geometry more suitable for meshing, resulting in the final models depicted in Figures 15 and 16.

Figure 15: Plantar Fascia Model From Gemagic

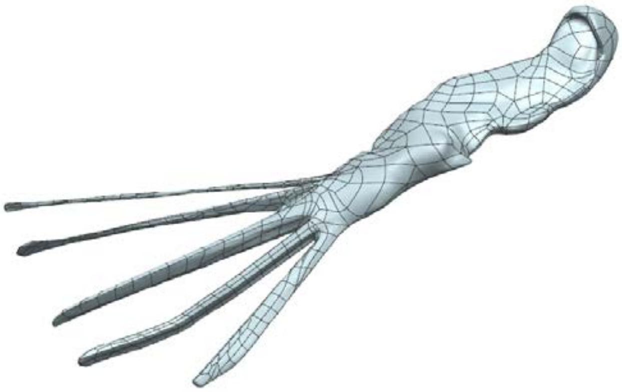

Figure 16: Plantar Fascia NURBS CAD Model

The soft tissue was cleaned up in a similar manner, beginning as shown in Figure 17 and resulting in the final model shown in Figure 18.

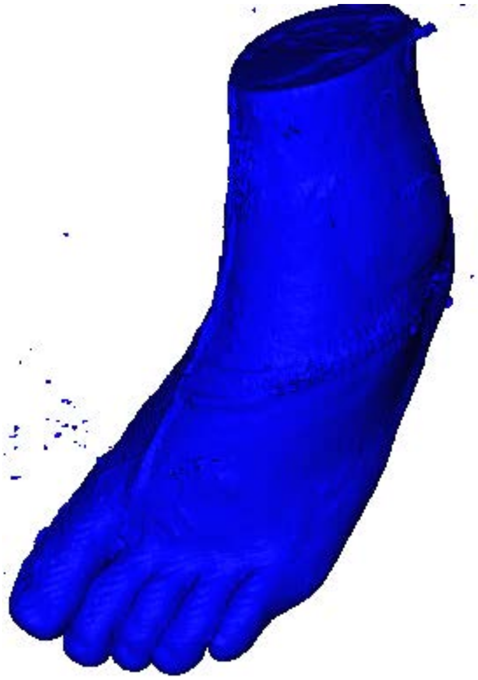

Figure 17: FIJI Rough Soft Tissue Model

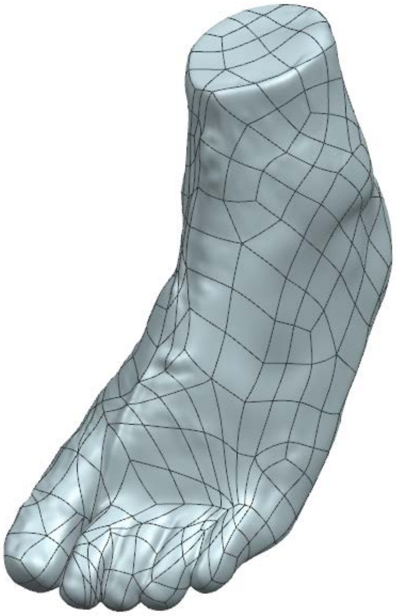

Figure 18: NURBS Surface Model of Soft Tissue

2.2.4. Final CAD Model

With each component created, the complete model was ready for assembly. First each bone and the plantar fascia were imported into the software. The creation method used in FIJI allowed for the bones to import into NX already in the proper location and orientation, creating the assembly shown in Figure 19.

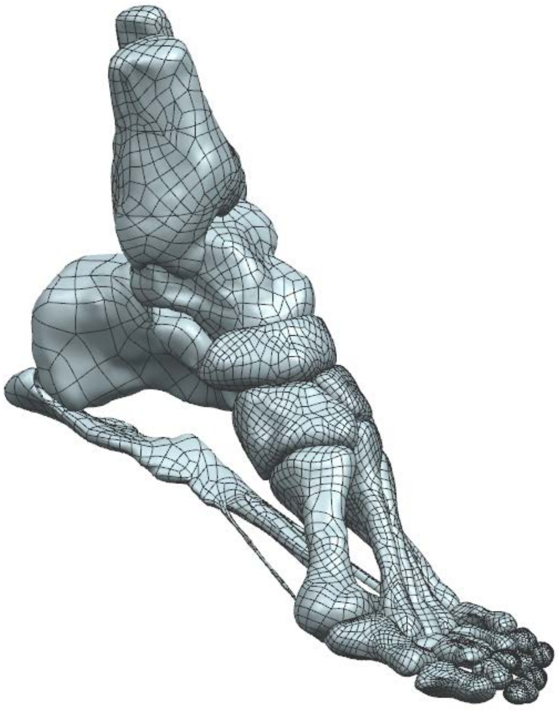

Figure 19: Bones and plantar Fascia CAD Model

To use the soft tissue, which was created as a solid body without any holes, the shapes of the bones were subtracted out of the soft tissue body to create cavities for the bones to sit in as shown in Figure 20.

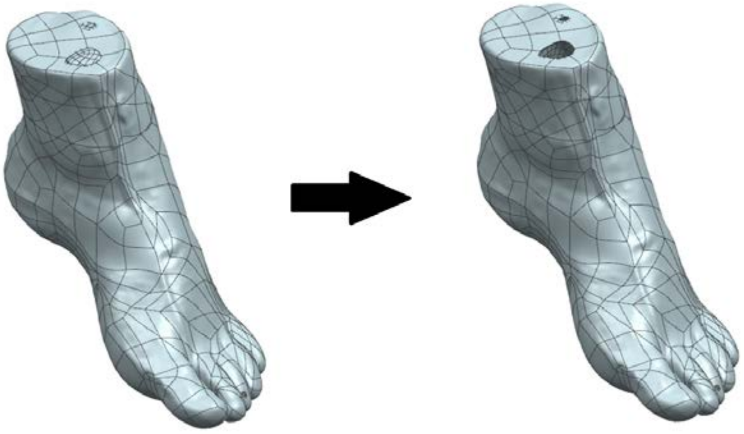

Figure 20: Soft Tissue Cavity Forming

Lastly, in order to create flat surfaces appropriate for applying boundary conditions, a plane was used to subtract the top portions of the soft tissue, tibia, and fibula from the overall models, resulting in the final model depicted in the Figure 21.

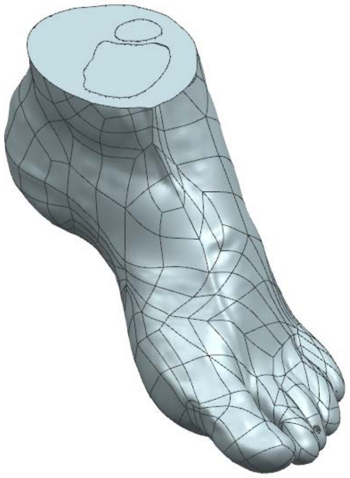

Figure 21: Final CAD Model

2.3. Finite Element Model

2.3.1. Mesh Generation

With the final CAD model assembled, the meshes for the finite element analysis could be generated. For each bone and the soft tissue, linear (4-node) tetrahedral elements were used for the analysis. The linear tetrahedral elements have been chosen for the 3-D geometry meshes to save on computation time. Future studies should endeavor to use non-linear tetrahedral elements for more accurate results. Figure 22 shows the resulting meshes and Table 1 summarizes the tetrahedral mesh data.

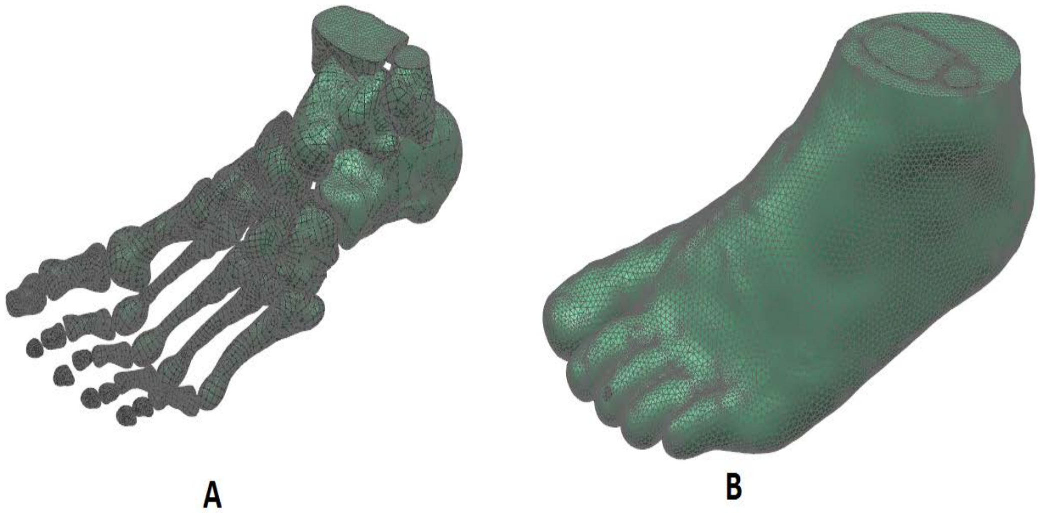

Figure 22: A) Bones Mesh B) Soft Tissue Mesh

Table 1: Element Data

Body	Number of Linear Tetrahedral Elements	Element Size (mm)
Calcaneus	28050	3.00
Talus	23223	3.13
Tibia	8915	2.74
Fibula	10506	2.42
Navicular	19305	1.99
Cuboid	21757	2.26
Lateral Cuneiform	17322	1.72
Middle Cuneiform	17333	1.43
Medial Cuneiform	17220	1.99
First Metatarsal	19978	2.19
Second Metatarsal	22537	1.65
Third Metatarsal	20038	1.71
Fourth Metatarsal	22158	1.58
Fifth Metatarsal	19360	1.83
Phalange 11*	18007	1.52
Phalange 12	18860	1.11
Phalange 21	7310	1.53
Phalange 22	4059	1.5
Phalange 23	1823	1.5
Phalange 31	9763	1.15
Phalange 32	2297	1.5
Phalange 33	2184	1.5
Phalange 41	12150	1.16
Phalange 42	2431	1.5
Phalange 43	2715	1.5
Phalange 51	13520	1.14
Phalange 52	2478	1.5
Phalange 53	2690	1.5
Soft Tissue	940097	3.02
Plantar Fascia	147546	1.7

*Here the first number following the Phalanges represents the metatarsal the phalange is connected to, and the second number represents the position, 1 being closest to the metatarsal (proximal), 3 being the furthest (distal) from the metatarsal.

In order to reduce computation time, the plantar fascia was also meshed using 4-node tetrahedral elements. However, additional measures were taken to guarantee that the results obtained were as accurate as possible. To ensure that the results were accurate, a mesh convergence study was performed until the change in the steady state results for a point near the calcaneus between iterations was less than 10%, as shown in Figure 23.

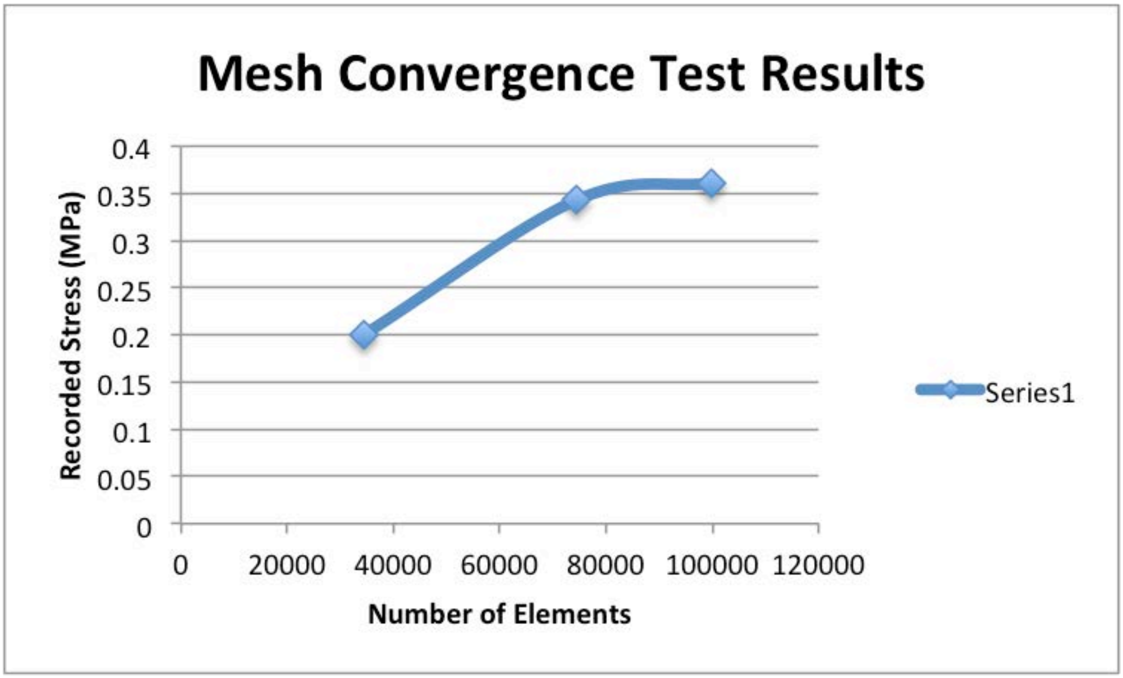

Figure 23: Mesh Convergence for Steady-State Results

The calcaneus region of the plantar fascia was chosen for the mesh convergence study as it is the area where the most pain is experienced for those with plantar fasciitis, and so is the region of interest for analysis. It was noted that the stress results tended to change drastically between neighboring elements near the connections to the metatarsals. This was likely due to the presence of sharp edges in the geometry. Therefore, the meshes were refined to be even denser in those regions so that there is a smoother stress gradient in the final results in those regions. This refinement was performed using NX's Mesh control functions, depicted in Figure 24 by the red triangles, resulting in a final mesh with 147,546 elements.

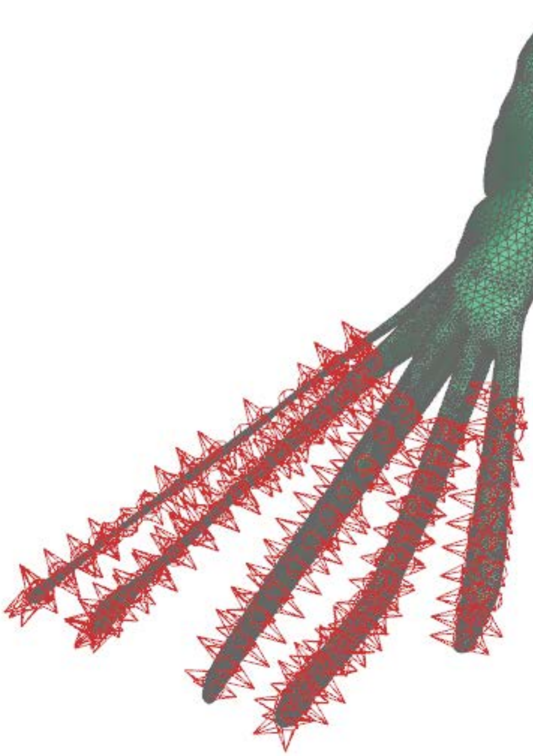

Figure 24: Plantar Fascia Mesh

Lastly, 1-D tension only rod elements with a cross sectional area of 18.4 mm^2 were used to model the ligaments as typical in literature such as [29]. The tension only property will be further elaborated in the next section. The rod elements were placed based on the locations described in [32]. These rod elements were connected at surface nodes on the bones to which the ligaments were attached. In total, 59 rod elements were created as seen in Figure 25 as the blue lines on the model.

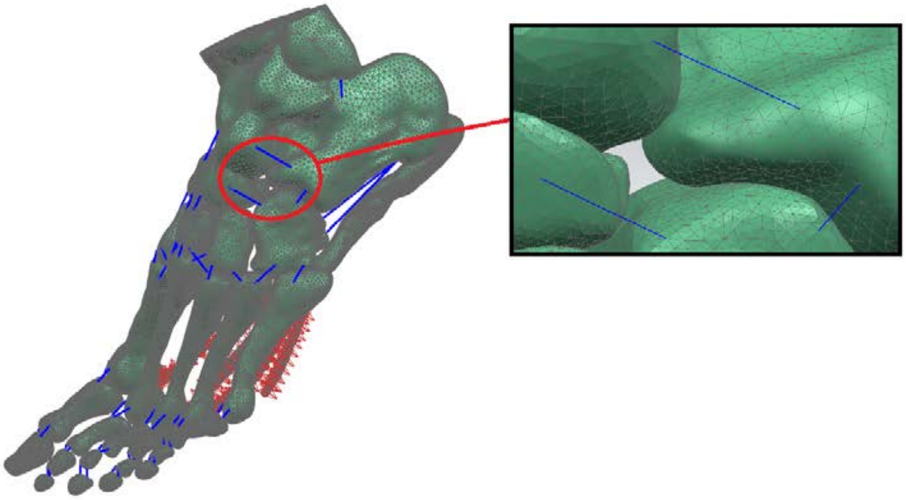

Figure 25: Ligament Rod Elements

2.3.2. Loading Conditions

Two loads were applied to the mesh. First, a downward force of 350 N was applied to the tibia and fibula, with half the load on each, to simulate the weight of the body for a person with a mass of approximately 70 kg. This loading is consistent with the physical loading of the model used in literatures such as [17]. This loading was applied as a uniform pressure distribution as depicted in Figure 26.

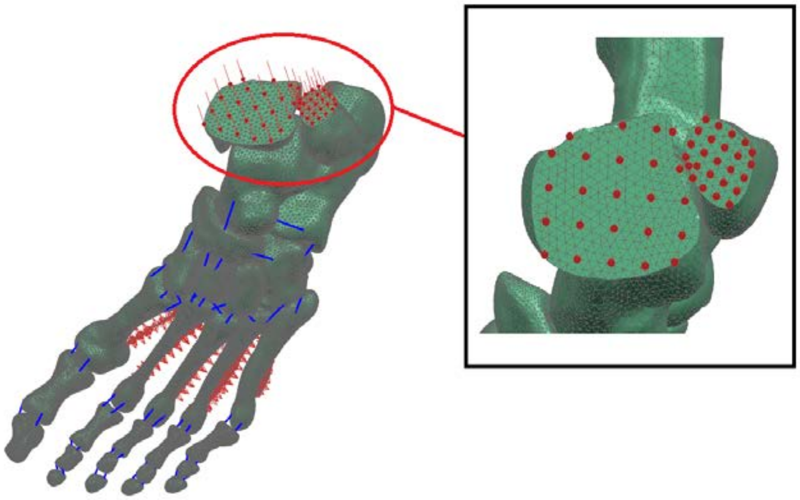

Figure 26: Loading on the Tibia and Fibula

The second loading is that of the tension from the Achilles' tendon on the calcaneus. This load was 50% of the weight applied to the foot (175 N) in the upward direction and distributed along the surface as an even pressure distribution as demonstrated in Figure 27 below, and is in agreement with that of [19].

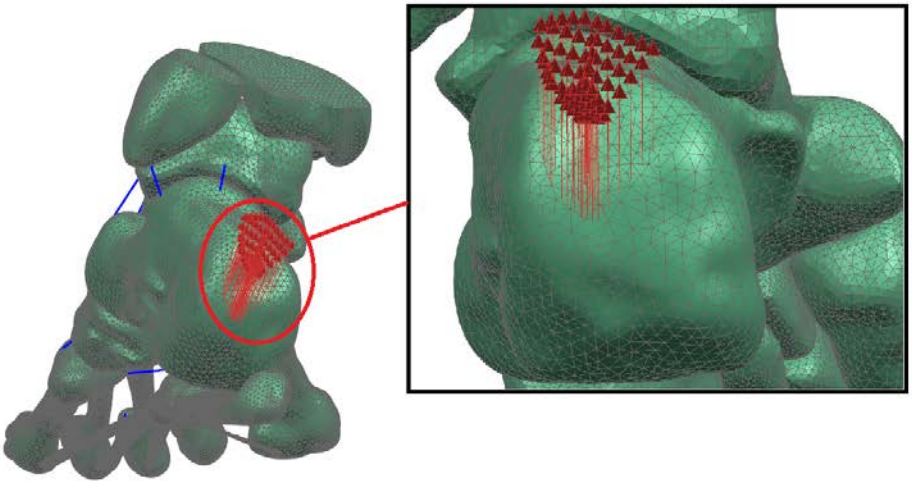

Figure 27: Achilles' Tendon Loading

2.3.3. Boundary Conditions and Contact Modeling

2.3.3.1. Displacement Constraint

Next, the model had to be properly constrained. To do this, the bottom of the foot was constrained to match the areas of the foot in contact with the ground while standing, according to a pressure distribution from literature for a standing position [17]. While the exact distribution would vary from person to person, constraining the foot in this manner relatively well represents the behavior of the foot's contact with the floor under loading. The sole of the foot was fixed in all directions $(x, y, z, \theta_x, \theta_y, \theta_z)$ as shown in Figure 28 (illustrated in the blue markers on the foot).

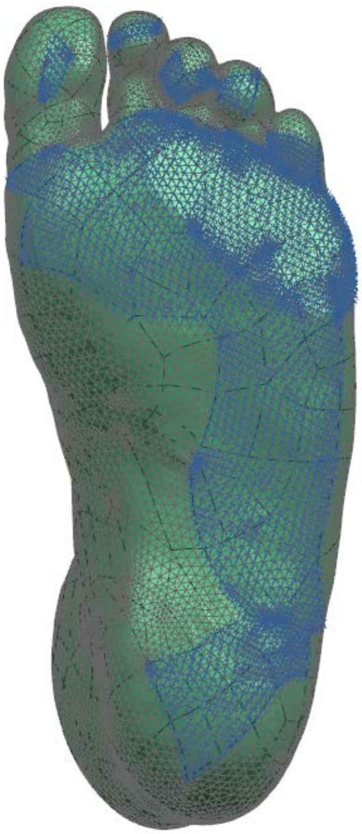

Figure 28: Constraints on the Sole of the Foot

2.3.3.2. *Contact Modeling*

The load transfer between the components of the foot is facilitated through the use of cartilage and tendons. Tendons were modeled as 1-D rod elements as will be discussed in the Material Parameters section. This section details the modeling of cartilage through the use of gluing constraints, as well as the gluing of bones to the soft tissue to hinder relative motion between the bones and soft tissue.

To enforce compressive loadings between bones and the soft tissue as facilitated by cartilage, the edges of touching bones were constrained via a rigid gluing constraint. These edges were paired via NX's automatic face pairing capabilities. Figure 29 shows the resulting glue constraints for the bones (represented by the yellow arrows), as well as the gluing constraint between the plantar fascia, metatarsals, and calcaneus.

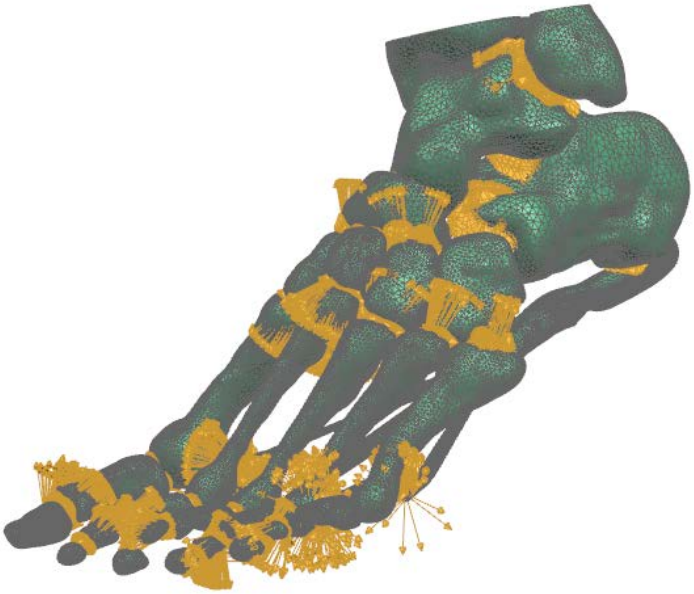

Figure 29: Glue Constraint Between Bones

This pairing method works well to ensure that the loading is transferred between bones; however, it eliminates any relative motion between the bones, and will increase the stresses at the contact regions.

The bones were also glued to the soft tissue cavities using the automatic face pairing command in NX. This was done to ensure that the bones could not have relative motion with the soft tissue. Figure 30 below shows the glue pairing (again represented by the yellow arrows) for the first metatarsal bone, wherein the entire surface of the bone has glue constraints matching it to the adjacent cavity in the soft tissue.

Figure 30: Glue Constraint to Soft Tissue

2.3.4. Solver Information

Analysis of the finite element model was carried out using NX solver 601- Advanced Nonlinear transient. The plantar fascia has a relaxation time (which is essentially the steady-state time) of 120 seconds [27]; therefore, the transient solver was run over a period of time of that length. The solver was set to do 100 steps with 1.2

seconds between steps. This was done so as to have a sufficiently small time step that would give a proper resolution in the transient results, while also keeping the total computation time to a reasonable amount. The simulation was run as a purely mechanical model with finite (large) strain formulations.

2.4. Material Property Data

2.4.1. Plantar Fascia

2.4.1.1. Hyperelastic Material Parameters

As discussed in section 1.2.2.4, the viscohyperelastic model of the present work requires material properties of both the elastic (steady-state) and viscous (transient) portions of the material behavior in order to fully characterize the viscohyperelastic behavior of the plantar fascia under loading. As in literature, such as [20], a 5-term incompressible Mooney-Rivlin material model was used for the elastic behavior of the plantar fascia. The incompressibility constant makes the volumetric constants D_{ij} be equal to zero. The values of C_{ij} are defined in Table 2 below and were input into the NX software as shown in Figure 31 as consistent with Cheng et al. [20].

Table 2: Plantar Fascia Material Parameters

Plantar Fascia Material Parameters (MPa)				
C_{01}	C_{10}	C_{11}	C_{02}	C_{20}
290.97	-222.1	4.7267	79.602	-1.1257

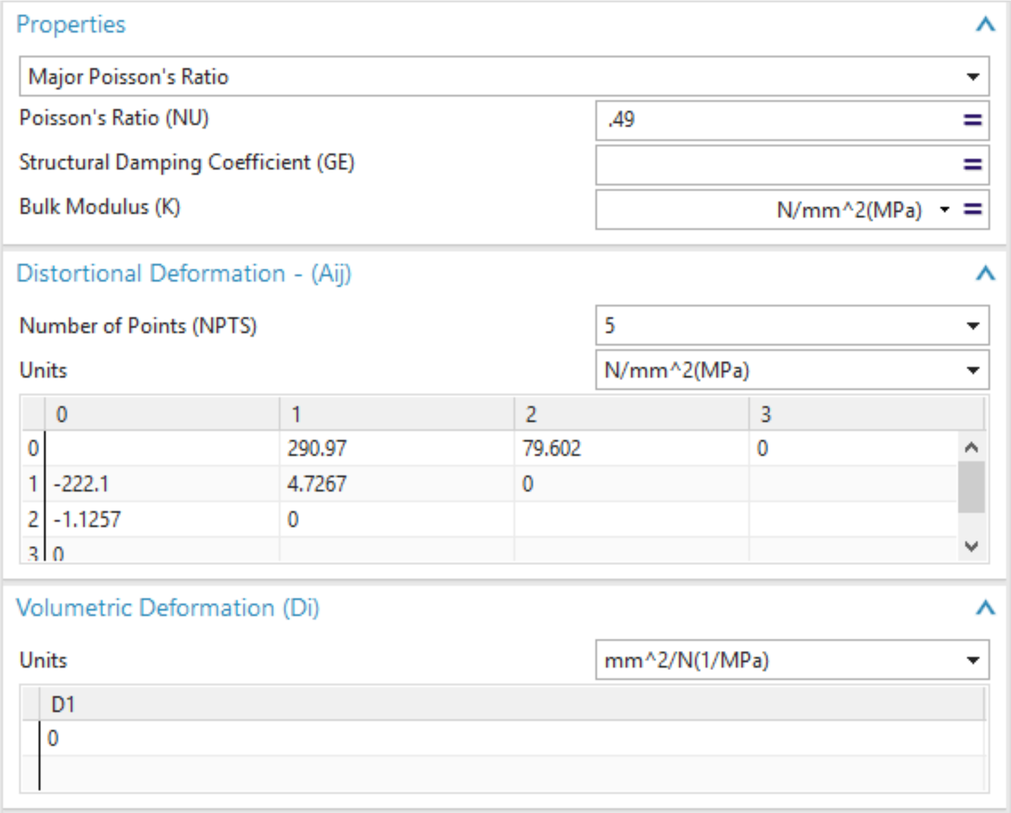

Properties

Major Poisson's Ratio

Poisson's Ratio (NU): .49

Structural Damping Coefficient (GE):

Bulk Modulus (K): N/mm^2(MPa)

Distortional Deformation - (Aij)

Number of Points (NPTS): 5

Units: N/mm^2(MPa)

	0	1	2	3
0		290.97	79.602	0
1	-222.1	4.7267	0	
2	-1.1257	0		
3	0			

Volumetric Deformation (Di)

Units: mm^2/N(1/MPa)

D1
0

Figure 31: Plantar Fascia Properties

Using the strain-energy function below and taking the derivative with respect to the stretch in the direction of loading for a tensile case, the stress for any given stretch value can be found.

$$W(\lambda) = C_{02}\left(2\lambda + \frac{1}{\lambda^2} - 3\right)^2 + C_{10}\left(\frac{2}{\lambda} + \lambda^2 - 3\right) + C_{20}\left(\frac{2}{\lambda} + \lambda^2 - 3\right)^2 + C_{01}(2\lambda + \frac{1}{\lambda^2} - 3) + C_{11}(2\lambda + \frac{1}{\lambda^2} - 3)(\frac{2}{\lambda} + \lambda^2 - 3) \tag{22}$$

Where

$$\sigma = \lambda \frac{dW(\lambda)}{d\lambda} \tag{23}$$

See Appendix A for the MATLAB code used to determine the stress at any specified strain value. To determine the parameters of β and τ, a strain of 8% was used due to the availability of experimental relaxation data values for that strain value being reported by Pavan et al. [27].

2.4.1.2. Viscoelastic Material Parameters

Recall from the viscoelastic theory section that the material parameters of β and τ are needed to characterize the transient behavior of the plantar fascia, where β is a proportionality constant that relates the transient strain energy density to that of the steady-state strain energy density, and τ is a time constant that relates to the time required to reach steady state. To obtain values of β and τ, data from literature was used [27]. The work of [27] was originally presented as a normalized ratio of the stress at a given time to the initially recorded stress. To derive the parameters of β and τ, the data plot presented by Pavan had to be denormalized for a given strain value. For this work, a strain value of 8% was used due to the availability of relaxation data in literature at that strain value from the work of Pavan et al. [27]. The steady state stress is approximately 24 MPa at a strain of 8%. Taking the final stress value to be 65% of the initial stress value as observed in Pavan et al.'s work, Figure 32 shows the denormalized plot [27].

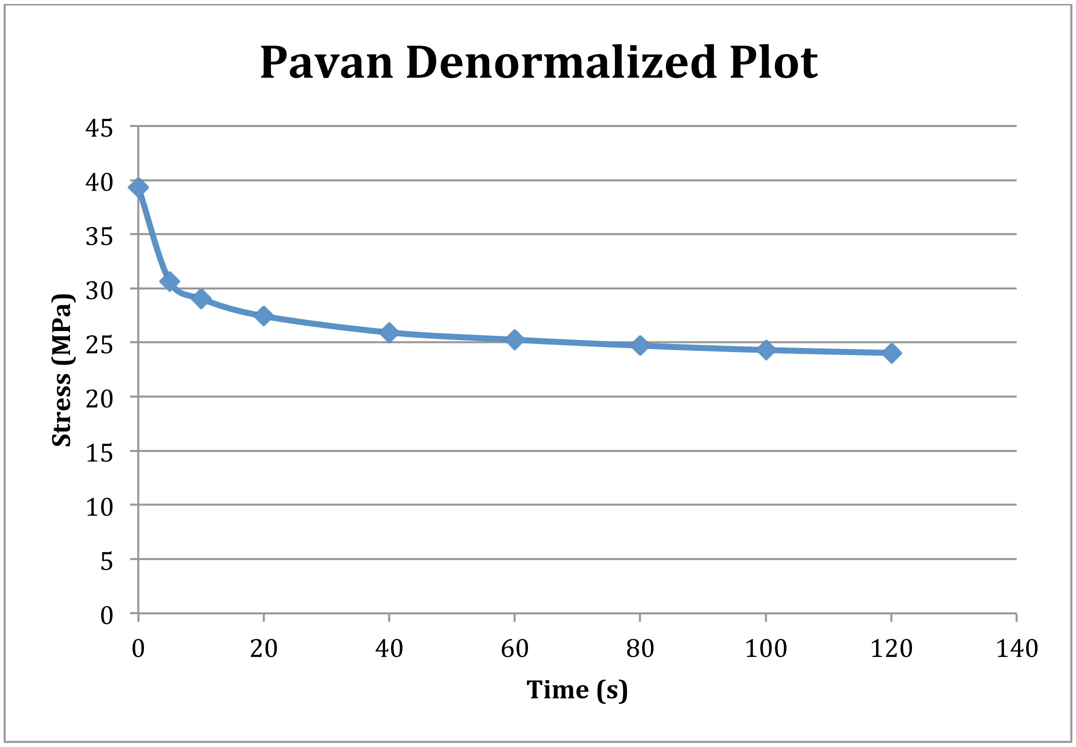

Figure 32: Denormalized Pavan Plot for 8% Strain

Curve fitting values of β and τ to this plot using the transient stress approximation of Equation 16 led to values of $\beta = 0.557$ and $\tau = 24$ seconds. These values are on a similar scale to the values found in [22], which used a different hyperelastic strain energy density, bringing validity to the present values of β and τ. NX does not have built in functionality to input viscoelastic properties, requiring the finite element code to be modified manually. Viscoelastic properties are added to the solver code through the use of the MATHEV command, which has the format shown in Table 3 [31].

Table 3: MATHEV Format Table

MATHEV	MID	SHIFT	C1	C2
	Beta	Tau	HGEN	USAGE

The parameters of the command are as follows. First, MID is the material identification number, which corresponds to the hyperelastic material to which the properties are being applied. Second, SHIFT, C1, and C2, and HGEN are parameters relating to thermal properties, and are set to zero (or left blank) by default for a mechanical process. Third, Beta and Tau are the values of β and τ of the material. Finally, the USAGE field indicates whether the strain energy is based on the dilatational strain energy, deviatoric strain energy, or both. For three-dimensional solids as in this case, the only value that NX allows is 0 (or leaving the spot blank) to make the strain energy based on the deviatoric behavior. The MATHEV command should be added to the solver code at the end of the Material Cards section, as illustrated in Figure 33 by the highlighted section of the figure.

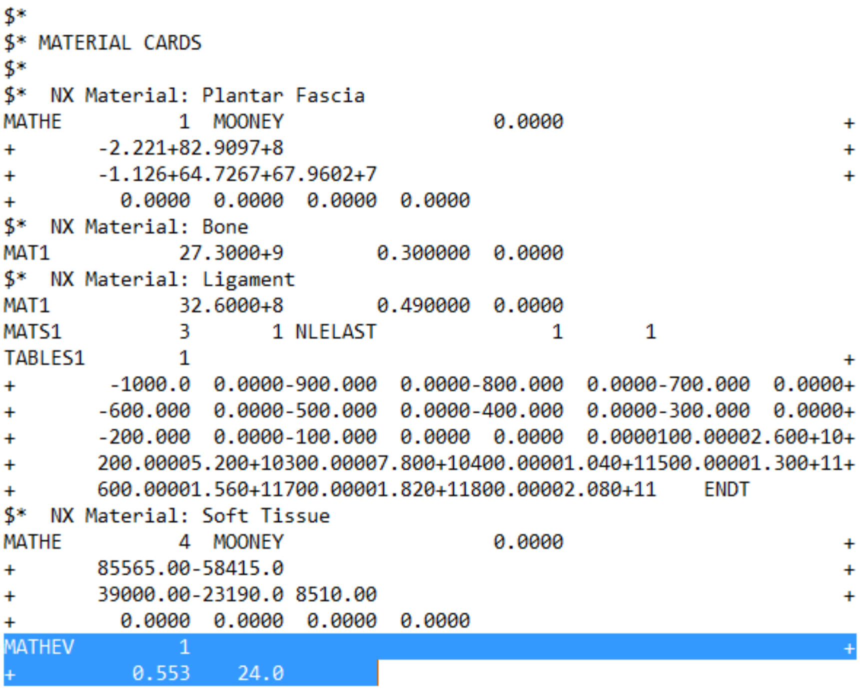

```
$*
$* MATERIAL CARDS
$*
$*  NX Material: Plantar Fascia
MATHE          1  MOONEY                  0.0000                        +
+       -2.221+82.9097+8                                                +
+       -1.126+64.7267+67.9602+7                                        +
+         0.0000  0.0000  0.0000  0.0000
$*  NX Material: Bone
MAT1           27.3000+9        0.300000  0.0000
$*  NX Material: Ligament
MAT1           32.6000+8        0.490000  0.0000
MATS1          3       1 NLELAST               1       1
TABLES1        1                                                        +
+        -1000.0  0.0000-900.000  0.0000-800.000  0.0000-700.000  0.0000+
+       -600.000  0.0000-500.000  0.0000-400.000  0.0000-300.000  0.0000+
+       -200.000  0.0000-100.000  0.0000  0.0000  0.0000100.00002.600+10+
+       200.00005.200+10300.00007.800+10400.00001.040+11500.00001.300+11+
+       600.00001.560+11700.00001.820+11800.00002.080+11    ENDT
$*  NX Material: Soft Tissue
MATHE          4  MOONEY                  0.0000                        +
+       85565.00-58415.0                                                +
+       39000.00-23190.0 8510.00                                        +
+         0.0000  0.0000  0.0000  0.0000
MATHEV         1                                                        +
+          0.553    24.0
```

Figure 33: MATHEV Command

2.4.1.3. Verification of Viscous Parameters in Finite Element Software

To test the validity of the model for finite element applications, a finite element model was created. Simple CAD geometry of a cube of volume 100^3 mm^3 was first created using Siemen’s NX as per [31]. Next, a mesh using 10-node tetrahedral elements of size 12 was applied to the body, using the same material properties as the plantar fascia. Convergence tests were done to ensure the accuracy of the results. One side of the cube was constrained, while the opposite edge was given a displacement value of 8 mm such that it corresponded with the 8% strain value of [27]. Figure 34 shows the cube with the described boundary and loading conditions applied prior to running the analysis.

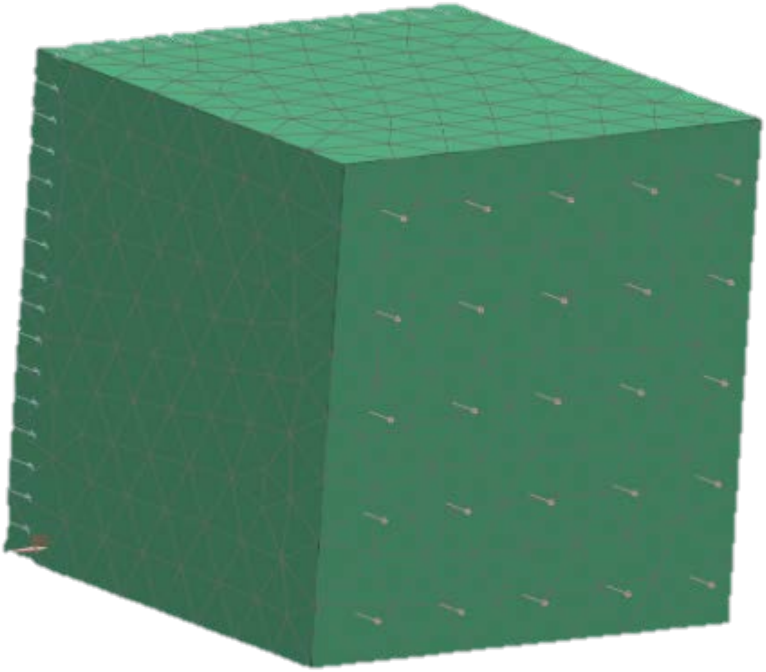

Figure 34: FEM Mesh and Applied Boundary Conditions

The simulation was solved using the 601,129 Advanced Nonlinear Transient solver while applying the MATHEV command as in Figure 33 with the viscoelastic parameters of the plantar fascia ($\beta = 0.556$ and $\tau = 24$ seconds). This resulted in the stress versus time plot shown in Figure 35.

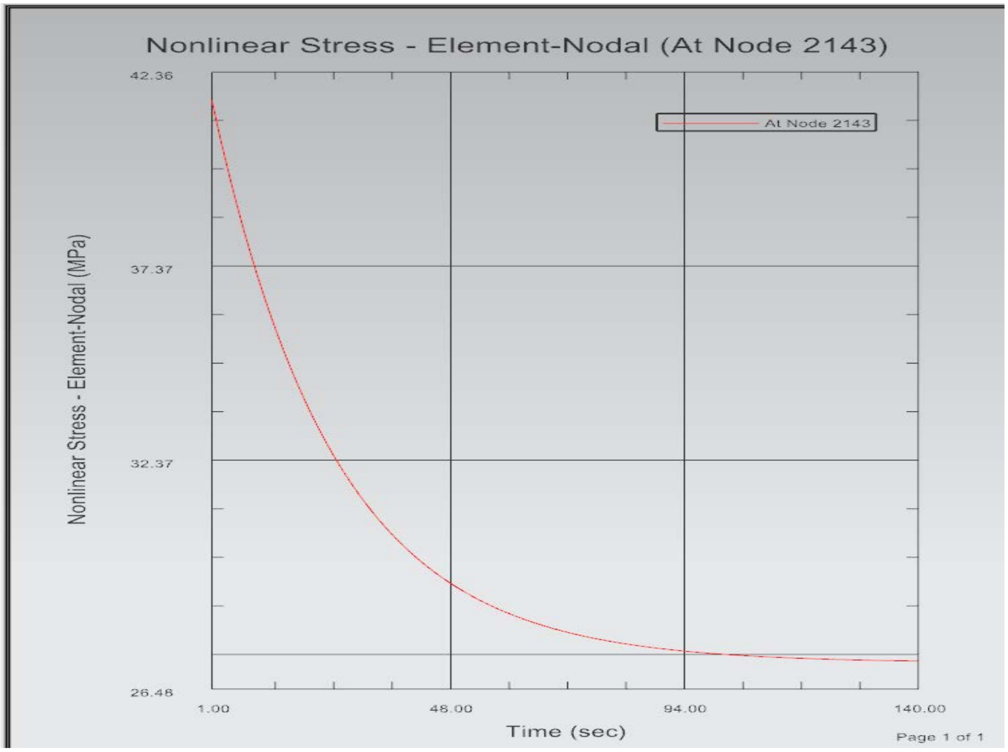

Figure 35: Stress vs. Time of Verification Model

This test model produces results that are almost identical to that of the theoretical stress plot depicted in Figure 32, showing that the solver produces accurate results. The only notable difference is that this analysis resulted in an equilibrium stress of 27 MPa for the strain value of 8% (computed using the MATLAB code in appendix A), which shows a slight divergence from the expected value computed numerically using the MATLAB code in appendix A, which resulted in an equilibrium stress of approximately 24 MPa. However, the results of the analysis are still within reason.

2.4.2. Bone, Soft Tissue, and Ligament Material Data

The bones, soft tissue, and ligaments were all modeled as elastic materials, with the bones and ligaments as linearly elastic and the soft tissue as non-linearly elastic. The bones were assigned a Young's Modulus of $E = 7{,}300\ MPa$ as in literature [17]. One notable comment on the bone's material properties is that this value does not factor in different values of Young's modulus for trabecular and cortical bone layers. Future research endeavors should seek to model the different types of bones for more accurate results.

The soft tissue was modeled as a non-linear elastic solid. Like the plantar fascia, a 5-term Mooney-Rivlin solid was used to characterize the soft tissue's behavior. Unlike the plantar fascia, the soft tissue was modeled as a compressible substance. This means that the dilatational material constant is non-zero in this case. Table 4 summarizes the material parameters for the soft tissue [17].

Table 4: Soft Tissue Material Parameters

Soft Tissue Material Parameters (MPa)					
C_{01}	C_{10}	C_{11}	C_{02}	C_{20}	D_1
-0.058415	0.085565	-0.02319	0.00851	0.039	3.65273

These properties were applied in the NX software as shown in Figure 36, noting that a Poisson's ratio was not specified due to the value of D taking its place.

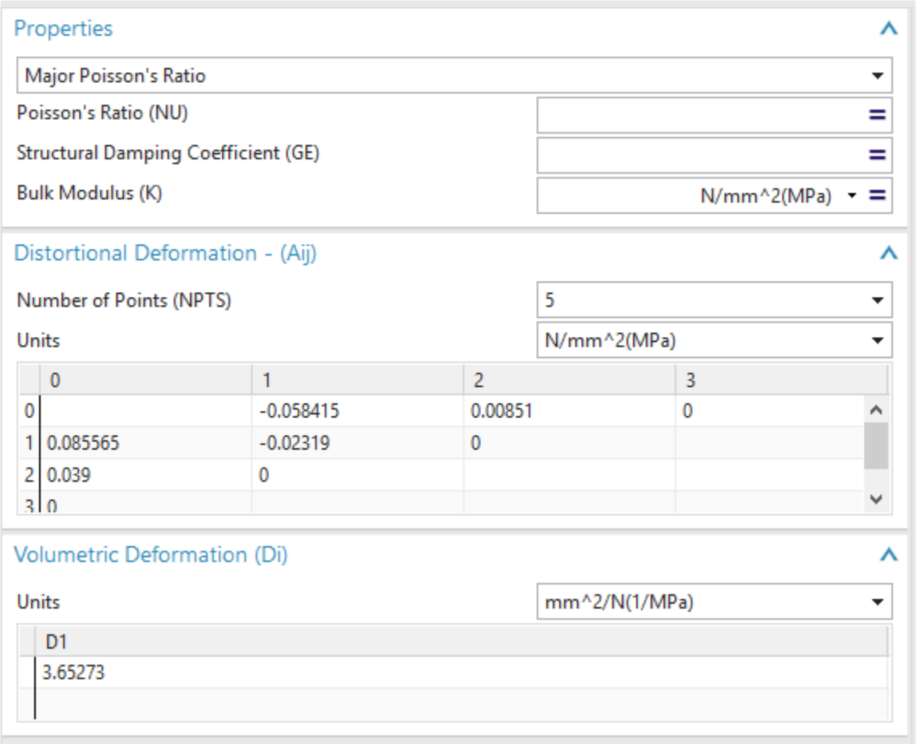

Properties

Major Poisson's Ratio

Poisson's Ratio (NU)

Structural Damping Coefficient (GE)

Bulk Modulus (K) N/mm^2(MPa)

Distortional Deformation - (Aij)

Number of Points (NPTS): 5

Units: N/mm^2(MPa)

	0	1	2	3
0		-0.058415	0.00851	0
1	0.085565	-0.02319	0	
2	0.039	0		
3	0			

Volumetric Deformation (Di)

Units: mm^2/N(1/MPa)

D1
3.65273

Figure 36: Soft Tissue Properties

As with the bones, the ligaments were modeled as linearly elastic. Unlike bones, ligaments primarily function only as tensile cables [20]. As a traditional rod element can have both tensile and compressive degrees of freedom, the stress-strain curve for the ligaments was modified to have only non-zero stress values for tensile strain values by editing the stress-strain curve as directed by NX’s advanced analysis guide as shown in Figure 37.

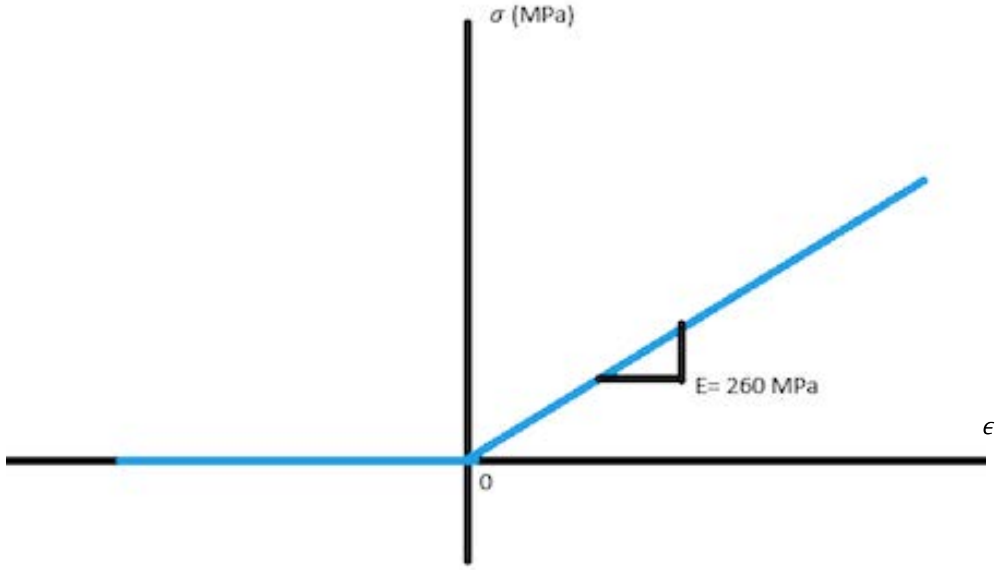

Figure 37: Ligament Stress vs. Strain Curve

Figure 37 illustrates that the stress was forced to be zero for negative strain values, causing the material to only carry loading in tension. A positive Young's Modulus of 260 MPa was chosen so as to be consistent with the work of Cheung et al. [17].

Chapter 3. Results, Analysis, and Conclusion

3.1. Results and Analysis

With the loading and boundary conditions applied, the finite element model was analyzed. Figures 38 and 39 present the overall stress and deformation results for the entire foot.

Figure 38: Von-Mises Stress Results for the Entire Foot

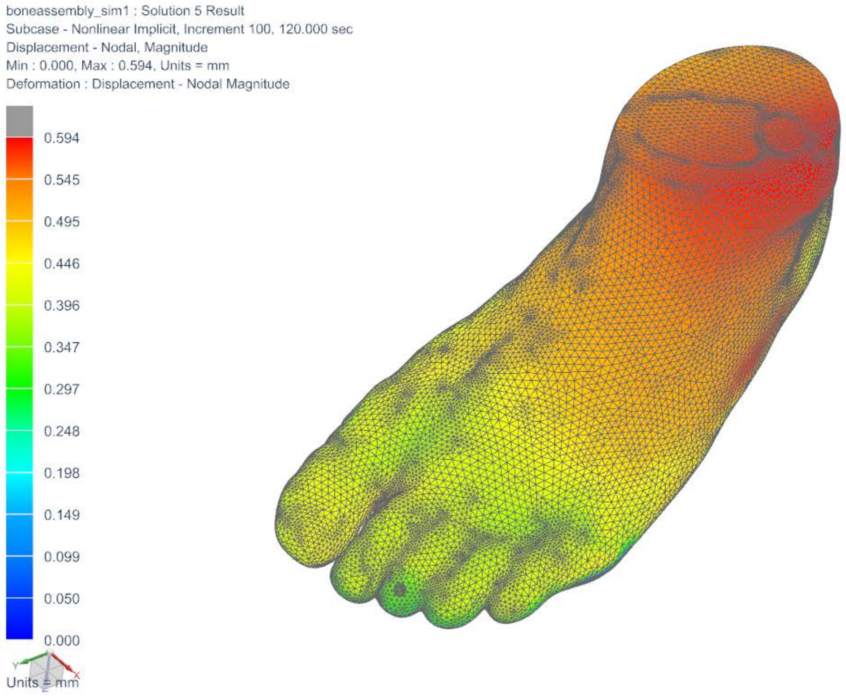

Figure 39: Displacement Magnitude Results for the Entire Foot

It can be seen from Figure 38 that there is a shift in the magnitude of stress between that of the soft tissue and the bones due to the differences in material properties and the way in which the loading was applied. Figure 39 illustrates that the bones and soft tissue displace together, showing that the glue constraint worked as intended. The results of each component of the model will now be presented in further detail.

3.1.1. Analysis of the Stresses on the Plantar Fascia

This section details the results of the plantar fascia. The peak steady-state von-Mises stresses were found to be at the edges where the plantar fascia meets the metatarsals and at the connection with the calcaneus. The peak stresses of the plantar fascia are shown in Figure 40, which presents the peak steady-state stress in the plantar fascia.

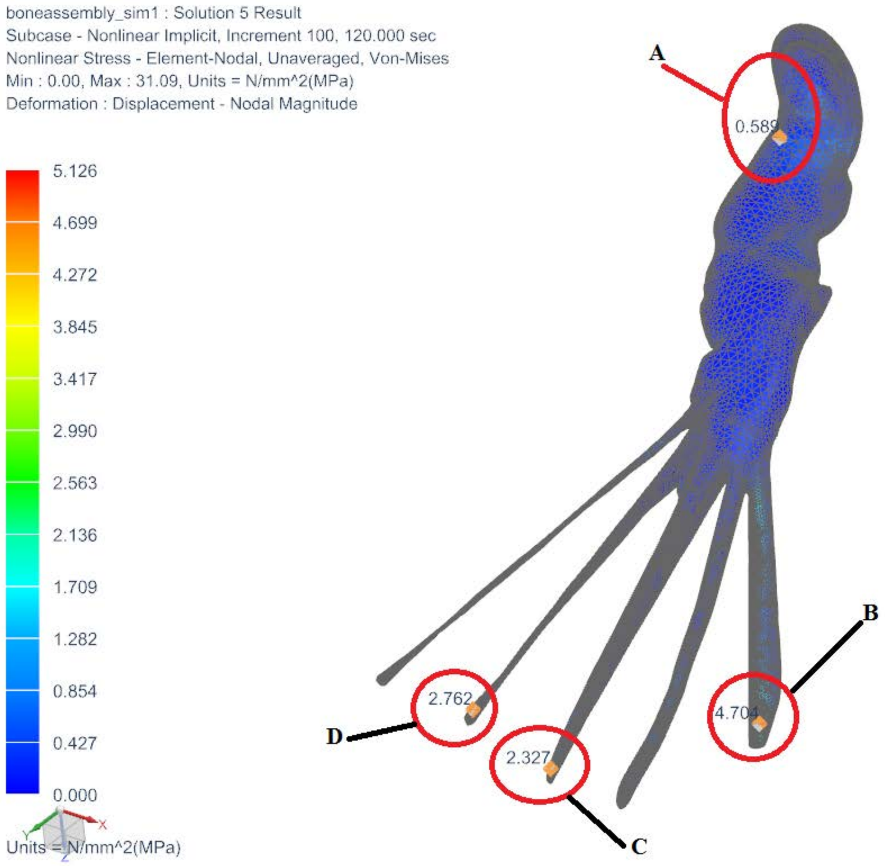

Figure 40: Plantar Fascia Peak von-Mises Stresses at Steady-State

Table 5 summarizes the peak stress values in the circled regions of interest.

Table 5: Peak Steady-State Stress Summary

Region	Peak Stress (MPa)
A	0.58
B	4.70
C	2.33
D	2.76

The higher stresses at the connections of the metatarsals can be attributed to the rigid glue constraint applied to connect the plantar fascia to the metatarsals. In addition, these regions contain geometry with some sharp edges that cause stress concentrations. The combination of the gluing constraints and sharp edges resulted in high stress values that extend beyond the physical reality at these regions, and are not as realistic. Further from these regions, the localized errors should decrease, causing the results to be more accurate. The region of the plantar fascia near the calcaneus is of interest due to it being the region of pain for people with plantar fasciitis. In the present model, this region has smooth edges that allow for more accurate results to be obtained even with the gluing constrain between it and the calcaneal tuberosity. The values at the calcaneus are of a similar scale to that found in Cheng et al.'s work [20]. The work of [20] studied the stresses and strains on the plantar fascia for a loading condition that only had tension from the Achilles tendon applied, and so a one-to-one comparison cannot be made. However, the results of the present work are on a similar scale to the work of Cheng et al., who presented a peak stress of approximately 0.6 MPa for a neutral dorsiflexion angle, so the present results are comparable [20]. Because the calcaneal region of the plantar fascia is where high levels of pain are typically experienced for those diagnosed with plantar fasciitis, the stresses at the calcaneus region were further analyzed.

The stress versus time curve for the highest stress on the plantar fascia in the heel region is depicted in Figure 41:

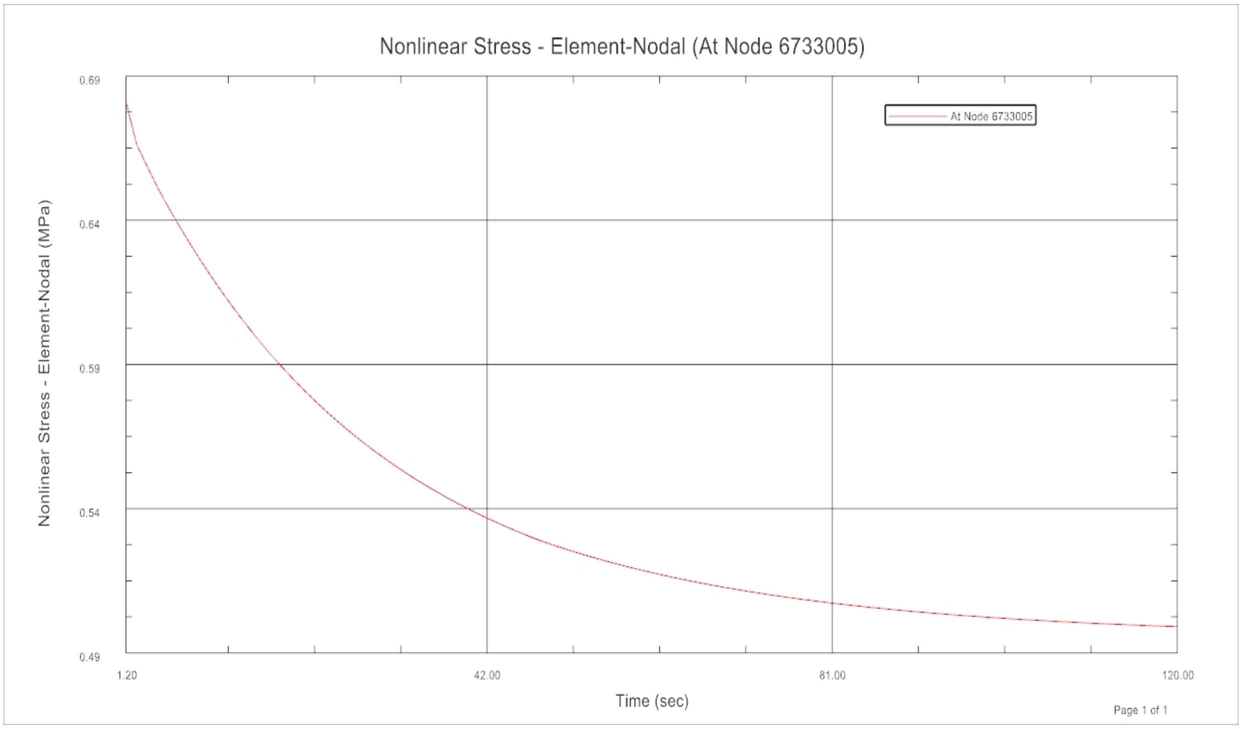

Figure 41: Stress vs. Time at Location of Interest

This figure implies a fairly significant difference between the initial and final stress values at that location, ranging from 0.68 MPa to 0.50 MPa across the relaxation time of 120 seconds. This range indicates that the stresses on the plantar fascia are significantly larger when the loading is first applied than when static equilibrium is reached. When considering the stresses that would occur during dynamic loading would be even higher, it becomes increasingly clear why plantar fasciitis is more likely to occur in running athletes.

3.1.2. Verification of Model: Comparison Between Static Model and Steady-State Results

To ensure that the steady-state response of the plantar fascia is appropriate, a static model was solved such that the viscous portion of the rheological modal was nonexistent. The static model's stress distribution results under the same loading and boundary conditions as the transient model are depicted in Figure 42:

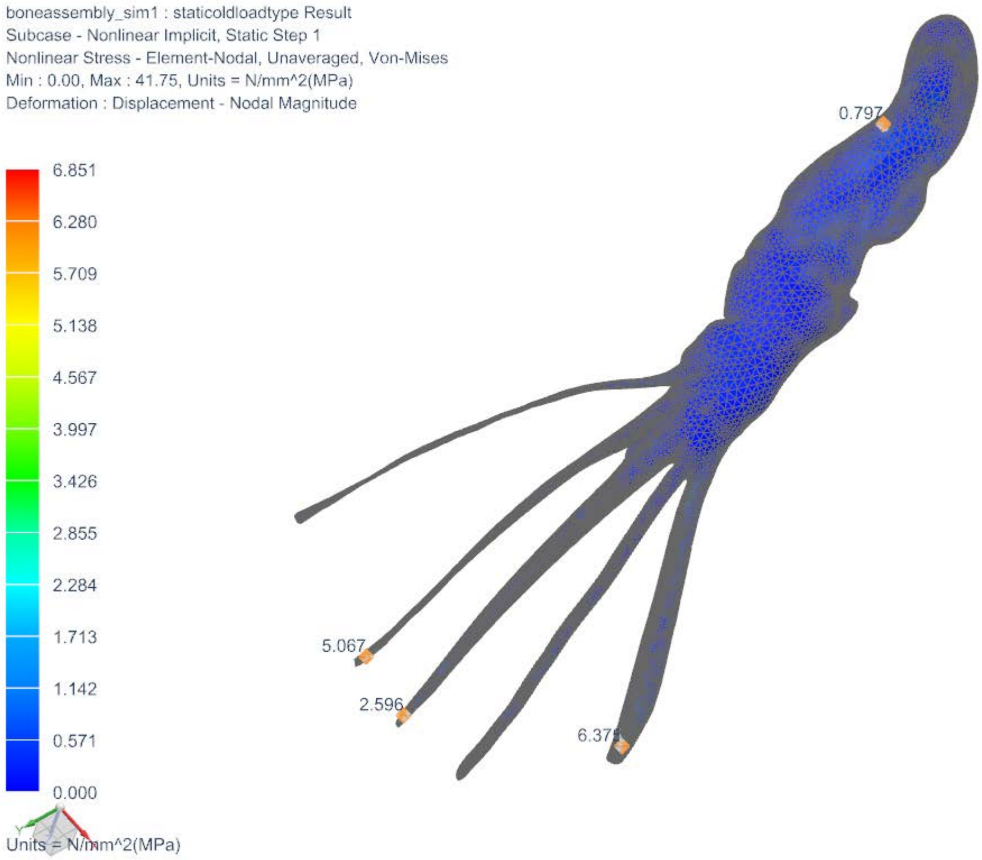

Figure 42: Plantar Fascia Peak von-Mises Stresses for Static Loading Conditions

It is evident from Figure 42 that the peak von-Mises stress for the static loading case recorded in the calcaneal region are very similar to the steady-state results of the transient model of Figure 40, as indicated by the highlighted stress value in the heel region in both figures. To further compare the two models, a sample node in the region of interest was chosen for comparison in both models. Figure 43 calls out the chosen comparison element in the heel region of the foot, and Figure 44 presents a side-by-side comparison of the stresses at that point for the steady-state and static solutions.

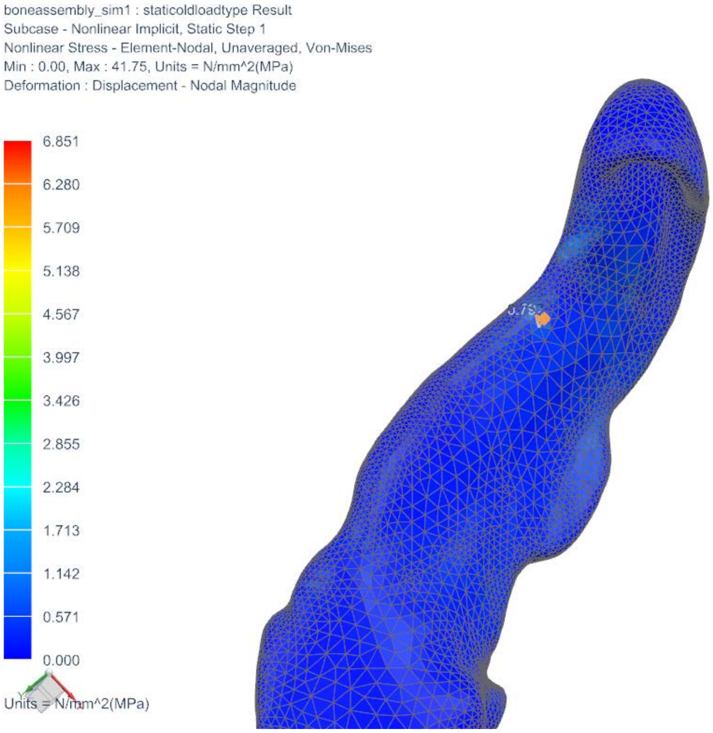

```
boneassembly_sim1 : staticoldloadtype Result
Subcase - Nonlinear Implicit, Static Step 1
Nonlinear Stress - Element-Nodal, Unaveraged, Von-Mises
Min : 0.00, Max : 41.75, Units = N/mm^2(MPa)
Deformation : Displacement - Nodal Magnitude
```

Figure 43: Comparison Point Location

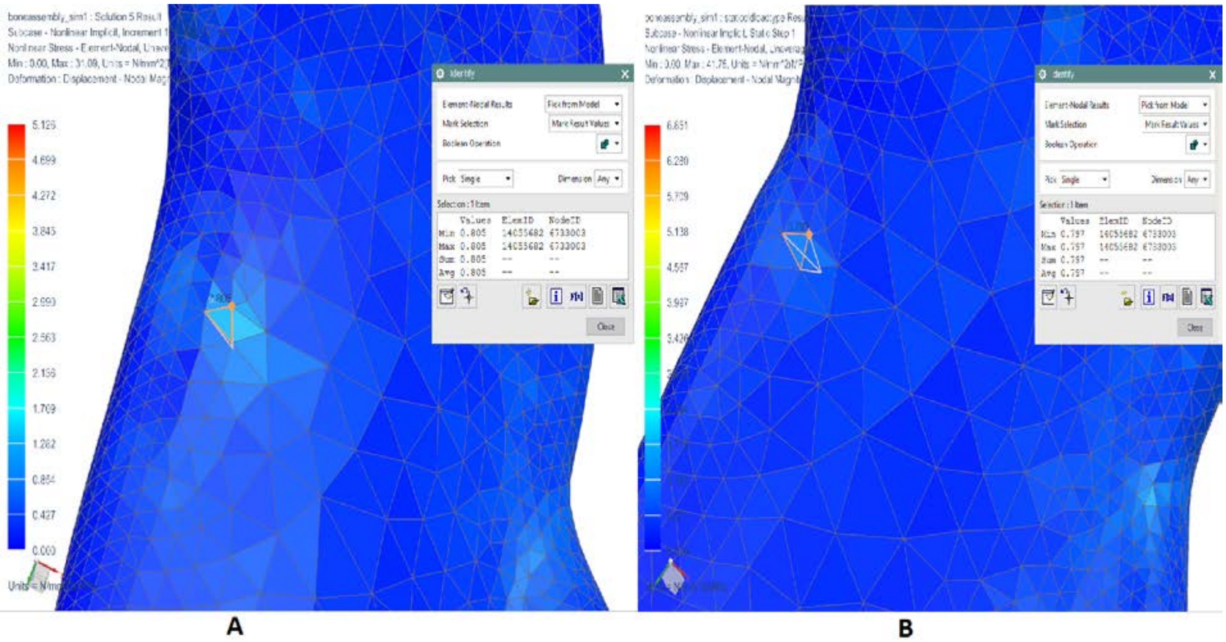

```
     Values  ElemID   NodeID
Min  0.805   14055682 6733003
Max  0.805   14055682 6733003
Sum  0.805   --       --
Avg  0.805   --       --
```

```
     Values  ElemID   NodeID
Min  0.797   14055682 6733003
Max  0.797   14055682 6733003
Sum  0.797   --       --
Avg  0.797   --       --
```

Figure 44: A) von-Mises Steady-State Stress Results vs. B) von-Mises Static Stress Results Comparison

The steady-state result is 0.805 MPa, and the static result is 0.797 MPa, differing by .99%. Given this, the two models are in agreement, and the transient model is converging appropriately.

3.1.3. Analysis of the Stresses on the Bones

The results of the stresses on the bones are discussed in this section. Figure 45 presents the magnitude of the displacements of the bones of the foot, and Figure 46 presents the von-Mises stresses for the bones of the foot.

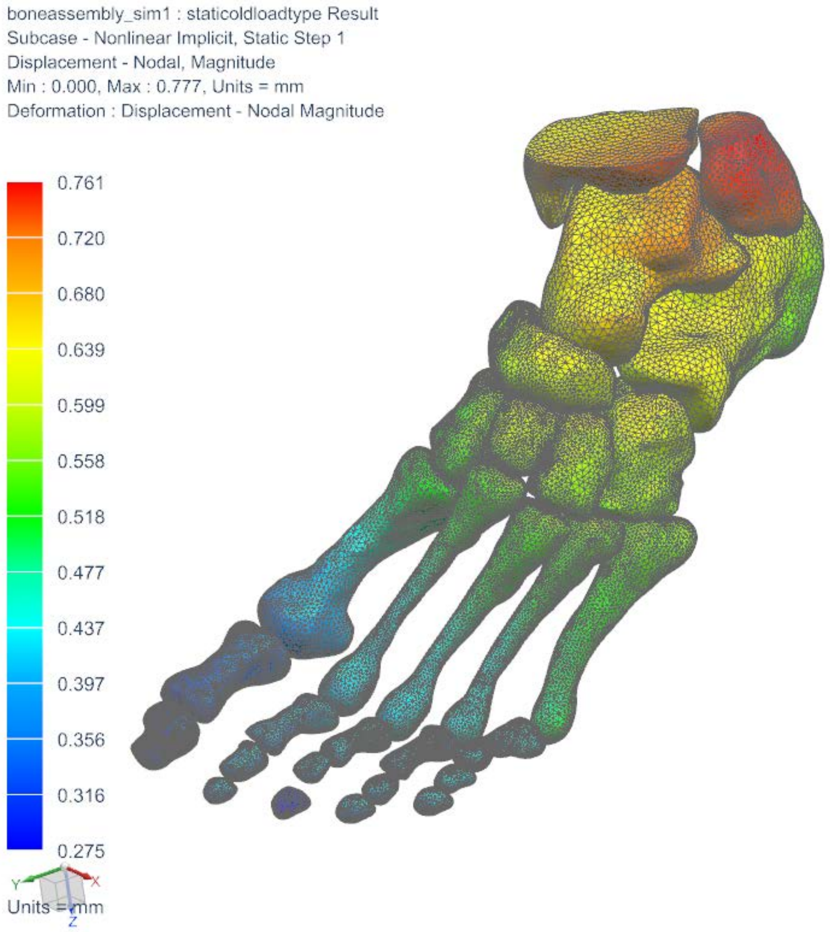

Figure 45: Bones Displacement Magnitude Results

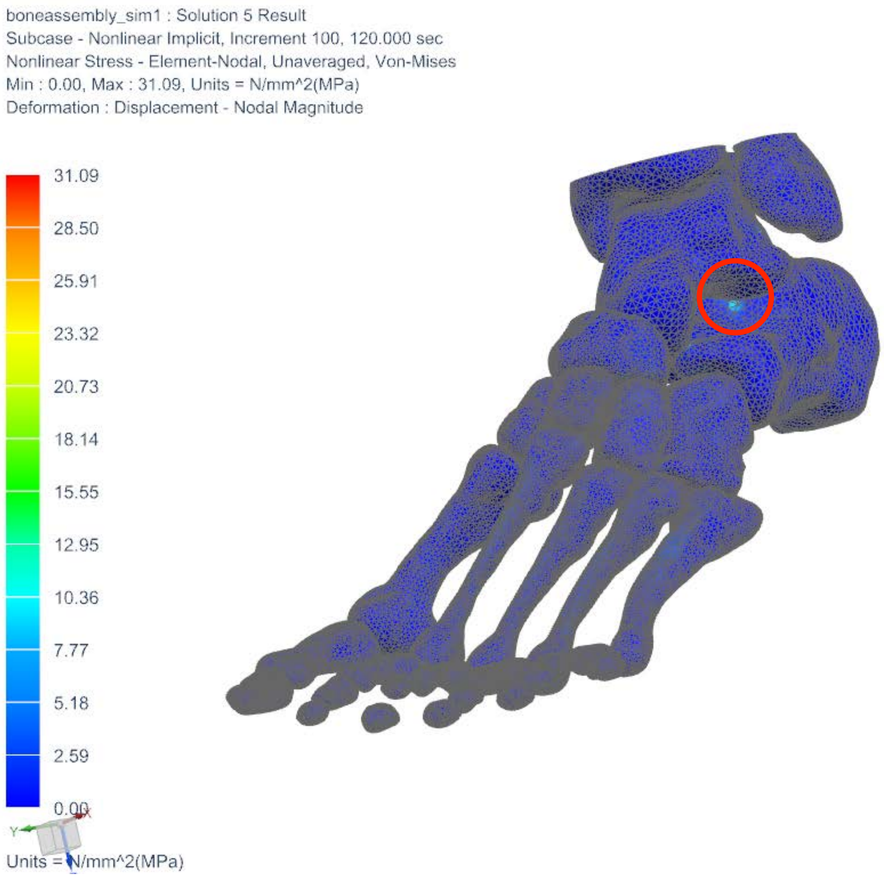

Figure 46: Von-Mises Stresses in the Bones Results

Figure 46 shows that the displacements of the bones are within reason, showing that none of the bones were displaced excessively, with a maximum displacement of .0761 mm. Figure 43 shows that the highest stresses appear where the calcaneus and talus come into contact (circled in red), with a reported stress of 31 MPa at that location. While the exact yield strength varies between bones, if the yield strength of cortical bone is taken to be 100 MPa at minimum based on that described in literature by Shin et al., the stresses are within reason in the present model, with a minimum factor of safety of 3.23 [43]. However, the rigid connections and ligaments cause localized stress concentrations, particularly on sharper edges. As one moves away from these concentrated stress regions, the results better mimic that of the actual foot and are therefore more reliable for analysis, and the factor of safety will increase. To illustrate this, the talus bone will be examined. Figure 47 illustrates the stresses on the talus.

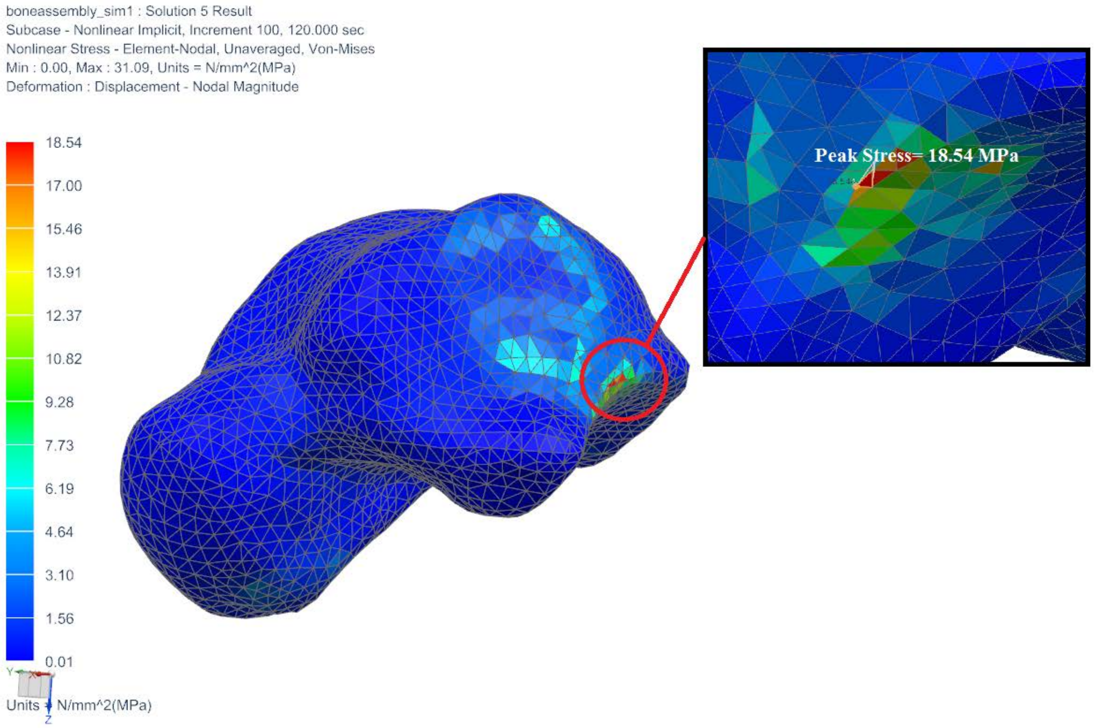

Figure 47: Talus Stress Distribution

As described, stress concentrations due to the gluing constraints have caused large increases in the stresses at these localized regions. In literature, the peak stress on the talus bone for the same weight was recorded to be 2.89 MPa [17]. In the present model, the peak stress is shown to be 18.54 MPa prior to removing erroneous localized errors. If one removes the unrealistic stress risers from the model, the stress distribution becomes much more realistic. Figure 48 illustrates this by showing the stress results that occur when the elements where stress concentrations occur are removed.

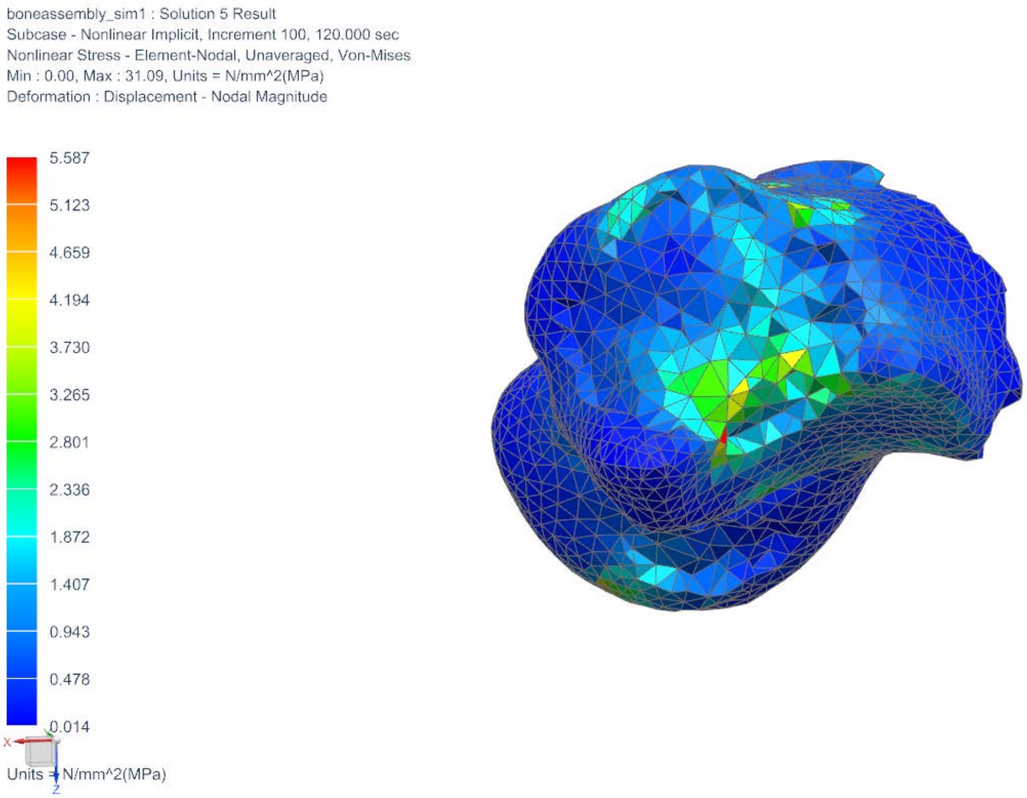

Figure 48: Talus Peak Stresses With Stress Risers Grayed Out

In Figure 48, the elements associated with the rigid connections to other bones were removed. It can be seen then that the majority of the stresses are at or below that which has been recorded in literature, with the maximum value (5.587 MPa) being well within the proper order of magnitude. Figure 49 shows the results of removing the areas of stress concentrations for every bone.

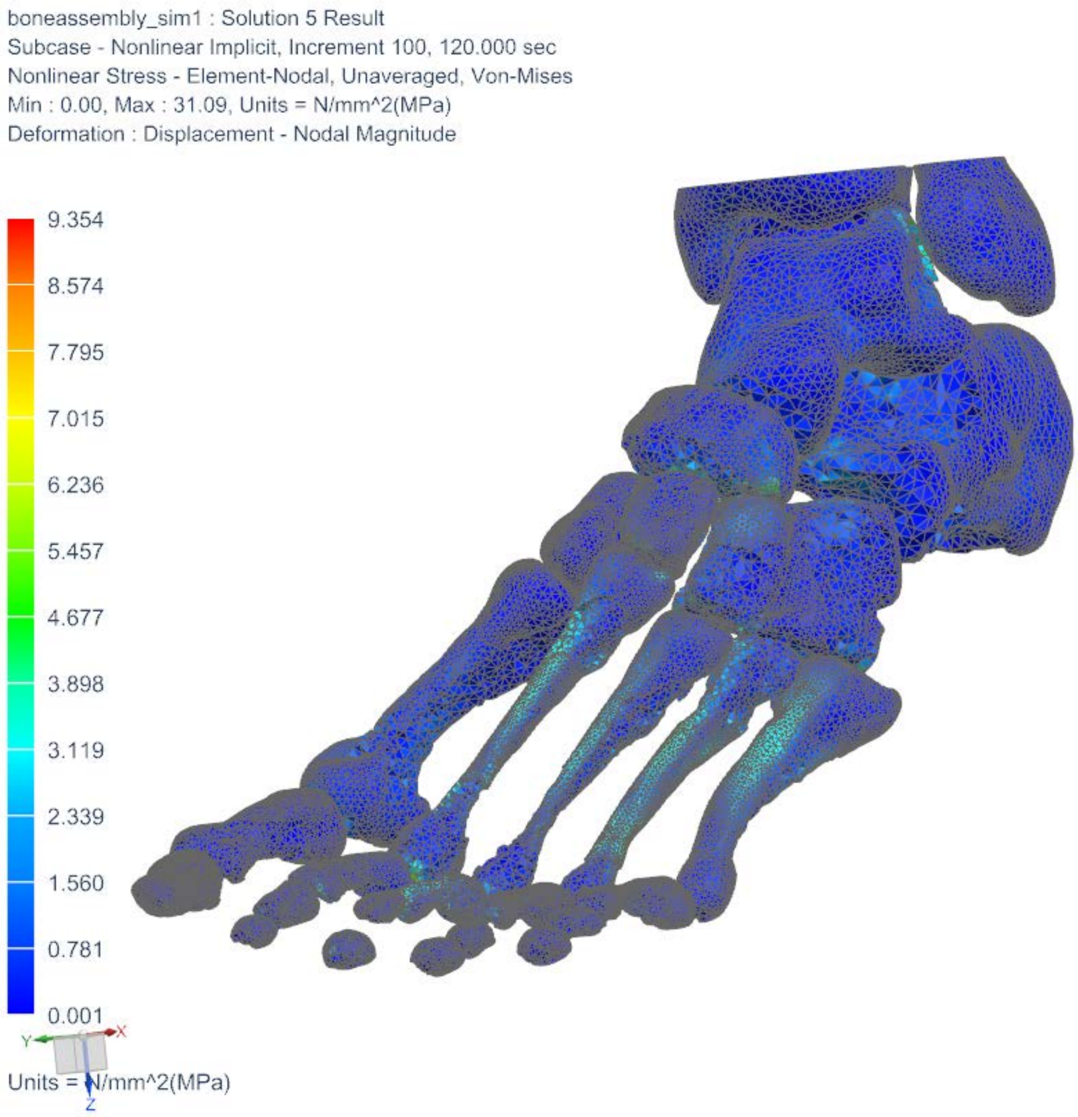

boneassembly_sim1 : Solution 5 Result
Subcase - Nonlinear Implicit, Increment 100, 120.000 sec
Nonlinear Stress - Element-Nodal, Unaveraged, Von-Mises
Min : 0.00, Max : 31.09, Units = N/mm^2(MPa)
Deformation : Displacement - Nodal Magnitude

Figure 49: Von-Mises Stress Results of the Bones with Stress Concentrations Removed

Figure 49 shows that the results become much more reasonable with the stress concentrations removed, with an overall factor of safety of 10.7. To reduce localized errors from stress risers, it is recommended that future research endeavors model cartilage between the bones and further refine the geometry to minimize sharp edges. Overall, the stresses on the bones appear to be on the proper order of magnitude as in literature and so should be suitable for analysis as long as the viewer examines points away from the peaks.

3.1.4. Analysis of the Stresses on the Soft Tissue

The results of the analysis for the soft tissue are presented in this section. Figures 49 and 50 present the stress and deformation results for the soft tissue at the steady-state time of 120 seconds.

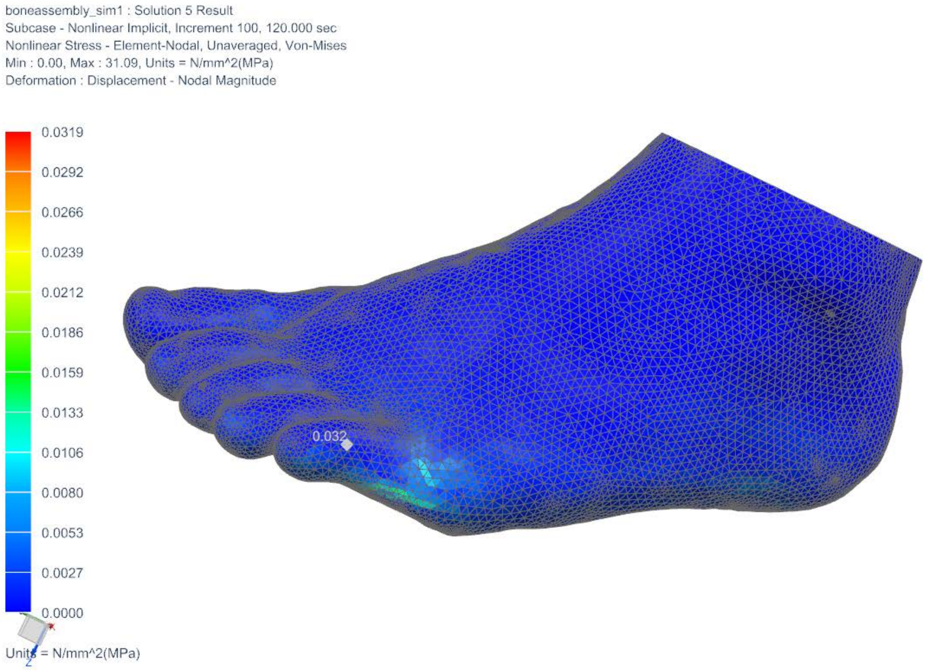

Figure 50: Von-Mises Stresses on the Soft Tissue

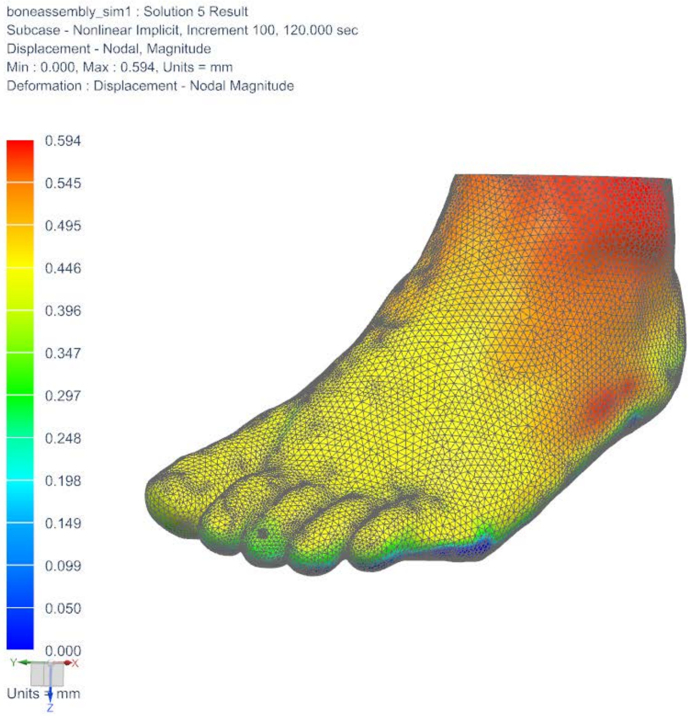

Figure 51: Displacement Magnitude Results of the Soft Tissue

As expected, the results peak at the connection points between the bones, in this case peaking at the area around the fourth metatarsal. The soft tissue modeled in this work is a combination of many different types of tissues, therefore, an exact yield strength is hard to quantify. However, if the yield strength is taken to be similar to that of collagen, which largely makes up soft tissue, as 50 MPa at minimum as in Pruitt et al. [33], the results are well within the failure range. The deformation results are similarly reasonable; no excessive deformations are present, with the peak amount being 0.6 mm near the top of the foot and the ankle complex, wherein the displacements decrease significantly as one gets closer to the fixed bottom of the foot.

3.2. Conclusion and Recommendations

A finite element model of the foot and plantar fascia was presented within. This simulation examined the plantar fascia as a viscohyperelastic solid, and the steady state results were consistent with previous experiments in literature. In this regard, the objective of creating a functional finite element model of the foot and plantar fascia was successfully met. This is a significant contribution to literature as a finite element model capable of analyzing the transient stresses of the plantar fascia had not been made prior to this work. The finite element model was created using geometry based on anatomic data available through NIH’s Visible Human Project, and was refined using the software Geomagic. After importing the geometry to NX, the geometry was meshed, loading and boundary conditions were applied, material properties were assigned, and the solver was run. Results of the model were all consistent with literature. The finite element method employed in this study yielded fruitful results that can be further employed in future studies to further characterize the transient behavior of the plantar fascia under loading. The present work shows a distinct increase in the stress on the plantar fascia when loading is first applied, giving empirical evidence that suggests why the pain is often at its highest in plantar fasciitis cases after periods of prolonged rest. While new methods of treating and preventing plantar fasciitis will require dynamic loading in order to be devised, this model lays the groundwork for such a model to be developed in the future.

This model represents the first step towards building models that can fully characterize the dynamic behavior of the plantar fascia, and relied on simplifications that created localized errors in the model, primarily due to the use of rigid gluing constraints between the bones used to model cartilage instead of a more sophisticated method. Future models should endeavor to model cartilage with physical CAD models, thereby creating a more realistic model that should improve the results. The rigid gluing constraints used in the model also stopped bones from moving relative to each other. Therefore, it is recommended that contact be modeled differently in future models to allow for the relative motion between bones. While the present work went to great labors to create smooth CAD models suitable for analysis, not all of the sharp edges were visually present, and therefore a few were still present in the final results. Future works can include further refinement of the CAD models, thereby reducing the likelihood of stress concentrations. Linear tetrahedral elements were used throughout this analysis; improved results may be obtained using 10-node tetrahedral elements, which may increase the accuracy of the obtained results. Lastly, the foot is a dynamic structure by nature, and therefore future models can examine the stresses during dynamic movements such as walking and running in order to characterize the stresses on the plantar fascia in day-to-day activities. Models with these improvements will give researchers greater insight into the causes of plantar fasciitis, allowing new ways to prevent plantar fasciitis in at-risk groups and treat it for those who are afflicted, through the use of novel orthotic designs.

References

1. Kim, W., & Voloshin, A. S. (1995). Role of plantar fascia in the load bearing capacity of the human foot. *Journal of Biomechanics*, *28*(9), 1025-1033.

2. Cheng, H. Y. K., Lin, C. L., Chou, S. W., & Wang, H. W. (2008). Nonlinear finite element analysis of the plantar fascia due to the windlass mechanism. *Foot & Ankle international*, *29*(8), 845-851

3. Riddle, D. L., Pulisic, M., & Sparrow, K. (2004). Impact of demographic and impairment-related variables on disability associated with plantar fasciitis. *Foot & Ankle international*, *25*(5), 311-317

4. McMillan, A. M., Landorf, K. B., Barrett, J. T., Menz, H. B., & Bird, A. R. (2009). Diagnostic imaging for chronic plantar heel pain: a systematic review and meta-analysis. *Journal of Foot and Ankle research*, *2*(1), 32.

5. Lutter, L. D. (1986). Surgical decisions in athletes' subcalcaneal pain. *The American Journal of Sports Medicine*, *14*(6), 481-485.

6. Gefen, A. (2002). Stress analysis of the standing foot following surgical plantar fascia release. *Journal of Biomechanics*, *35*(5), 629-637.

7. Carlson, R. E., Fleming, L. L., & Hutton, W. C. (2000). The biomechanical relationship between the tendoachilles, plantar fascia and metatarsophalangeal joint dorsiflexion angle. *Foot & Ankle International*, *21*(1), 18-25.

8. Pavan, P. G., Stecco, C., Darwish, S., Natali, A. N., & De Caro, R. (2011). Investigation of the mechanical properties of the plantar aponeurosis. *Surgical and Radiologic Anatomy*, *33*(10), 905-911.

9. Jacob, S., & Patil, M. K. (1999). Three-dimensional foot modeling and analysis of stresses in normal and early stage Hansen's disease with muscle paralysis. *Journal of Rehabilitation Research and Development*, *36*(3), 252.

10. Chu, T. M., Reddy, N. P., & Padovan, J. (1995). Three-dimensional finite element stress analysis of the polypropylene, ankle-foot orthosis: static analysis. *Medical Engineering & Physics*, *17*(5), 372-379.

11. Huerta, J. P., Garcia, J. M. A., Matamoros, E. C., Matamoros, J. C., & Martinez, T. D. (2008). Relationship of body mass index, ankle dorsiflexion, and foot pronation on plantar fascia thickness in healthy, asymptomatic subjects. *Journal of the American Podiatric Medical Association*, *98*(5), 379-385.

12. Spears, I. R., Miller-Young, J. E., Waters, M., & Rome, K. (2005). The effect of loading conditions on stress in the barefooted heel pad. *Med Sci Sports Exerc*, *37*(6), 1030-1036.

13. Yu, J., Cheung, J. T. M., Fan, Y., Zhang, Y., Leung, A. K. L., & Zhang, M. (2008). Development of a finite element model of female foot for high-heeled shoe design. *Clinical Biomechanics*, *23*, S31-S38.

14. Camacho, D. L., Ledoux, W. R., Rohr, E. S., Sangeorzan, B. J., & Ching, R. P. (2002). A three-dimensional, anatomically detailed foot model: a foundation for a finite element simulation and means of quantifying foot-bone position. *Journal of Rehabilitation Research and Development*, *39*(3), 401.

15. Knapp, A., Schonning, A., Stagon, S., & Livingstong, B. (Winter 2016). Development of 3D Geometry of the Foot for FE Plantar Fasciitis Study. *Journal of Management and Engineering Integration*.

16. Jackson, S. A. (Ed.). (2005). Cross-sectional imaging made easy.

17. Cheung, J. T. M., Zhang, M., Leung, A. K. L., & Fan, Y. B. (2005). Three-dimensional finite element analysis of the foot during standing—a material sensitivity study. *Journal of biomechanics*, *38*(5), 1045-1054.

18. Cheung, J. T. M., Zhang, M., & An, K. N. (2004). Effects of plantar fascia stiffness on the biomechanical responses of the ankle–foot complex. *Clinical Biomechanics*, *19*(8), 839-846.

19. Cheung, J. T. M., Zhang, M., & An, K. N. (2006). Effect of Achilles tendon loading on plantar fascia tension in the standing foot. *Clinical Biomechanics*, *21*(2), 194-203.

20. Cheng, H. Y. K., Lin, C. L., Wang, H. W., & Chou, S. W. (2008). Finite element analysis of plantar fascia under stretch—the relative contribution of windlass mechanism and Achilles tendon force. *Journal of Biomechanics, 41*(9), 1937-1944.

21. Antunes, P. J., Dias, G. R., Coelho, A. T., Rebelo, F., & Pereira, T. (2011). Nonlinear 3D foot FEA modeling from CT scan medical images. *Computational Vision and Medical Image Processing*, 135-145.

22. Natali, A. N., Pavan, P. G., & Stecco, C. (2010). A constitutive model for the mechanical characterization of the plantar fascia. *Connective Tissue Research*, *51*(5), 337-346.

23. Sconfienza, L. M., Silvestri, E., Orlandi, D., Fabbro, E., Ferrero, G., Martini, C., Sardanelli, F., & Cimmino, M. A. (2013). Real-time sonoelastography of the plantar fascia: comparison between patients with plantar fasciitis and healthy control subjects. *Radiology, 267*(1), 195-200.

24. Wu, C. H., Chang, K. V., Mio, S., Chen, W. S., & Wang, T. G. (2011). Sonoelastography of the plantar fascia. *Radiology*, *259*(2), 502-507.

25. Jiang, Y., Li, G. Y., Qian, L. X., Hu, X. D., Liu, D., Liang, S., & Cao, Y. (2015). Characterization of the nonlinear elastic properties of soft tissues using the supersonic shear imaging (SSI) technique: inverse method, ex vivo and in vivo experiments. *Medical Image Analysis*, *20*(1), 97-111.

26. Chaudhry, H., Huang, C. Y., Schleip, R., Ji, Z., Bukiet, B., & Findley, T. (2007). Viscoelastic behavior of human fasciae under extension in manual therapy. *Journal of Bodywork and Movement Therapies*, *11*(2), 159-167.

27. Pavan, P. G., Stecco, C., Darwish, S., Natali, A. N., & De Caro, R. (2011). Investigation of the mechanical properties of the plantar aponeurosis. *Surgical and Radiologic Anatomy*, *33*(10), 905-911.

28. Pavan, P. G., Pachera, P., Stecco, C., & Natali, A. N. (2014). Constitutive modeling of time-dependent response of human plantar aponeurosis. *Computational and Mathematical methods in medicine*, *2014*.

29. Fung, Y. C. (2013). Biomechanics: mechanical properties of living tissues.

30. Holzapfel, G. A. (1996). On large strain viscoelasticity: continuum formulation and finite element applications to elastomeric structures. *International Journal for Numerical Methods in Engineering*, *39*(22), 3903-3926.

31. Siemens, P. L. M. (2008). Software Inc. *NX Nastran User's Guide*.

32. Gray, H. (2009). *Gray's anatomy: with original illustrations by Henry Carter*. Arcturus Publishing.

33. Pruitt, L. A., & Chakravartula, A. M. (2011). Mechanics of biomaterials: fundamental principles for implant design.

34. Martins, P. A. L. S., Natal Jorge, R. M., & Ferreira, A. J. M. (2006). A Comparative Study of Several Material Models for Prediction of Hyperelastic Properties: Application to Silicone-Rubber and Soft Tissues. *Strain*, *42*(3), 135-147.

35. Malvern, L. E. (1969). Introduction to the Mechanics of a Continuous Medium.

36. Mooney, M. (1940). A theory of large elastic deformation. *Journal of Applied Physics*, *11*(9), 582-592.

37. Rivlin, R. S. "Large elastic deformations of isotropic materials. IV. Further developments of the general theory." *Philosophical Transactions of the Royal Society of London A: Mathematical, Physical and Engineering Sciences* 241, no. 835 (1948): 379-397.

38. Schonning, A., Oommen, B., Ionescu, I., & Conway, T. (2009). Hexahedral mesh development of free-formed geometry: The human femur exemplified. *Computer-Aided Design*, *41*(8), 566-572.

39. National Institute of Health and US National Library of Medicine, "The visible human project," 2009. http://www.nlm.nih.gov/research/visible/visible_human.html

40. Schindelin, J., Arganda-Carreras, I., Frise, E., Kaynig, V., Longair, M., Pietzsch, T., ...& Tinevez, J. Y. (2012). Fiji: an open-source platform for biological-image analysis. *Nature Methods*, *9*(7), 676-682.

41. Manual, G. U. (2002). Raindrop Geomagic. *Research Triangle, NC, USA.*

42. Hollister, S. M. (1997). The dirty little secrets of hull design by computer. *New Wave Systems Inc*.

43. Shin, J., Yue, N., & Untaroiu, C. D. (2012). A finite element model of the foot and ankle for automotive impact applications. *Annals of Biomedical Engineering, 40*(12), 2519-2531.

Appendix A

```
%Mooney-Rivlin Calculator
%Parameters are defined
c10=-222.1;
c01=290.97;
c20=-1.1257;
c11=4.7267;
c02=79.602;
%Paramters defined as variables, stretch defined as variable x
syms x c10 c01 c20 c11 c02
% First and Second Invariants Defined

y=((x^2)+(2/x))
z=((2*x)+(x^-2))
%Strain Energy Defined
f1=((c10*(y-3))+(c01*(z-3))+(c11*(y-3)*(z-3))+((c20*((y-
3)^2)))+((c02*((z-3)^2))))
%Derivative Taken
sigma=x*diff(f1)
%sigma@x= sigma(x) for any x value
```

Vita

Alexander Knapp is a research and teaching assistant in the Mechanical Engineering Program at the University of North Florida. He is an author of two publications, with three more in progress. After graduating from the University of North Florida, Alexander will attend the University of Florida to pursue a PhD in Mechanical Engineering, and aspires to become a professor following the completion of his education.

Publications:

Knapp, A., Schonning, A., Stagon, S., & Livingston, B. (2016). Viscous Effects of the Plantar Fascia Under Static Loading**.** Unpublished manuscript, Mechanical Engineering, University of North Florida, Jacksonville, United States
Expected Submission: April 2017.

Knapp, A., Schonning, A., Stagon, S., & Livingston, B. (2016). Viscohyperelastic Material Model of the Plantar Fascia for FEM Applications**.** Unpublished manuscript, Mechanical Engineering, University of North Florida, Jacksonville, United States
Expected Submission: March 2016.

Carlyle, P., Buxton, R., **Knapp, A**., Aceros, J., & Stagon, S. (2016). Characterization of Electrical and Mechanical Properties of Low Temperature Silver Nanorod Bonds. Unpublished manuscript, Mechanical and Electrical Engineering, University of North Florida, Jacksonville, United States
Submitted October 2016

Knapp, A., Schonning, A., Stagon, S., & Livingston, B. (Winter 2016). Development of 3D Geometry of the Foot for FE Plantar Fasciitis Study. *Journal of Management and Engineering Integration*.

Stagon, S., **Knapp, A**., Elliott, P., & Huang, H. (2016). Metallic Glue For Ambient Environments Making Strides. *Advanced Materials & Processes*.